TITLE: Distinct adaptations revealed by unbiased proteomic analysis of autophagy cargos in the brain in PINK1 and LRRK2 models of Parkinson's disease

AUTHORS: Goldsmith J[1,6], Ordureau A[2,3], Stavoe AKH[1,4], Boecker CA[1,5], Arany M[1], Harper JW[2,6], Holzbaur ELF[1,6,7].

[1] Department of Physiology, University of Pennsylvania Perelman School of Medicine, Philadelphia PA 19104 USA
[2] Department of Cell Biology, Blavatnik Institute, Harvard Medical School, Boston, MA, 02115 USA
[3] Current address: Cell Biology Program, Sloan Kettering Institute, Memorial Sloan Kettering Cancer Center, New York, NY, 10065 USA
[4] Current address: Department of Neurobiology and Anatomy, McGovern Medical School, University of Texas Health Science Center at Houston, Houston, TX 77030
[5] Current address: Department of Neurology, University Medical Center Goettingen, 37077 Goettingen, Germany
[6] Aligning Science Across Parkinson's (ASAP) Collaborative Research Network, Chevy Chase, MD.
[7] Lead Contact

ORCID:
JG: https://orcid.org/0000-0002-6935-1744
AO: https://orcid.org/0000-0002-4924-8520
AKHS: https://orcid.org/0000-0002-4073-4565
CAB: https://orcid.org/0000-0001-9701-5273
JWH: https://orcid.org/0000-0002-6944-7236
ELFH: https://orcid.org/0000-0001-5389-4114

Lead Contact and Corresponding Author:

Erika L. F. Holzbaur
Department of Physiology
University of Pennsylvania Perelman School of Medicine
415 Curie Boulevard
Philadelphia, PA 19104 USA
(215) 573-3257
holzbaur@pennmedicine.upenn.edu

ABSTRACT

Autophagy is a conserved and essential cellular degradation and recycling process that is required to maintain neuronal homeostasis. Genetic and pathological evidence suggest that autophagy is disrupted in Parkinson's disease (PD), a prevalent and progressive neurodegenerative disease, yet how changes in autophagy contribute to disease pathogenesis is unclear. To better understand the cellular impacts of disrupted autophagy on neuronal function, we used unbiased proteomics to compare the cargos degraded by basal autophagy in two different mouse models of PD. We isolated autophagic vesicles from the brains of PINK1 knock-out mice and LRRK2^{G2019S} knock-in mice, and further compared these data to observations from young and old mice. We find evidence for the upregulation of adaptive pathways to remove proteins and organelles in PINK1$^{-/-}$ and LRRK2^{G2019S} mice. In PINK1$^{-/-}$ mouse brain, impaired mitophagy leads to increased expression of components of the autophagic machinery as well as increased expression of selective adaptors for mitochondrial autophagy independent of PINK1/Parkin, including BCL2L13. In LRRK2^{G2019S} mice, we find that the impairments to autophagosome trafficking and acidification lead to increased cargo secretion. We further compared these data sets to proteomic data comparing young and old mice. In aged mice, we find decreased engulfment of lysosomes and increased engulfment of α-synuclein, a key component of pathogenic Lewy bodies found in PD. Together, these findings highlight the engagement of distinct compensatory pathways to maintain homeostasis in the brain upon disruption of either stress-induced or basal autophagic pathways, and we begin to identify how age-related changes may place further stress on autophagy's ability to maintain homeostasis.

INTRODUCTION

Autophagy is an evolutionarily conserved process for the clearance and recycling of proteins and organelles. Neurons have a unique dependence on autophagy, as impairment of this pathway leads to either neurodevelopmental or neurodegenerative phenotypes [1–3]. Cellular, genetic, and pathological data point to two major types of autophagy in neurons. Acute stress induces the targeting of dysfunctional organelles or aggregated proteins for turnover, in regulated pathways for mitophagy, lysophagy and aggrephagy, among other mechanisms [4]. These pathways generally involve damage-sensing, leading to induction of a downstream response. For example, mitochondrial damage leads to the stabilization of PINK1 kinase on the outer mitochondrial membrane (OMM), which in turn triggers a feedforward activation of the E3 ubiquitin ligase Parkin, leading to widespread ubiquitination of mitochondrial proteins and recruitment of ubiquitin-binding receptors such as OPTN that serve as a platform leading to the engulfment of the damaged organelle by a double-membrane autophagosome [5–8]. Similarly, in lysophagy, lysosomal membrane permeabilization that cannot be repaired via the ESCRT pathway leads to ubiquitination of proteins within the lysosomal membrane, followed by the recruitment of receptors including TAX1BP1 and p62/SQSTM1, and again the engulfment via a locally formed autophagosome [9,10].

In addition to these stress-induced mechanisms, there is robust cellular and in vivo evidence for a requirement of basal autophagy in neurons [11–13]. Autophagosomes form constitutively at synaptic sites and the axon terminus, engulfing diverse cargos into double-membrane autophagosomes. Newly formed autophagosomes then undergo a stereotypical pattern of highly regulated transport toward the soma, driven by the molecular motor cytoplasmic dynein. Defects in this transport impede the degradation of engulfed cargos. A notable example occurs in neurons expressing the most common familial mutation in Parkinson's disease (PD), the G2019S mutation in LRRK2. Pathological mutations in LRRK2 kinase induce hyperactivity, leading to hyper-phosphorylation of RAB proteins that are known LRRK2 kinase targets [14], and key regulators of vesicle trafficking pathways [15]. Elevated LRRK2 activity is sufficient to disrupt both the transport and the maturation of autophagic vesicles in the axon, leading to a block in autophagic degradation [16].

To better understand how autophagy supports normal neuron function, we used proteomics to identify the major cargos engulfed by autophagic vesicles in the brain under basal conditions, and found that mitochondrial fragments and synapse-related proteins were the prominent cargos of this homeostatic pathway. Western blotting and live imaging studies of induced human neurons and primary rodent neurons confirmed that these cargos were highly enriched in autophagic vesicles in neurons [17].

Next, we sought to understand how autophagic cargo might be altered in the context of PD, which is tightly linked to disrupted autophagy. PD is a progressive neurodegenerative disease primarily affecting dopaminergic neurons in the substantia nigra pars compacta. It presents as a movement disorder in patients with an average age of onset at 60. 15% of PD cases are familial, but in both familial and sporadic PD the most common risk factor is age, with disease severity correlating with age [18]. There have been many links of disrupted autophagy to PD. Abnormal autophagosome are accumulated in post-mortem patient brain tissue independent of etiology [19]; familial mutations in the genes encoding PINK1 and Parkin impair the selective autophagic degradation of damaged mitochondria, and mutations in LRRK2 impair autophagosome trafficking and maturation. Functional autophagy is responsible for clearing α-synuclein aggregates that can form the characteristic pathological Lewy bodies found in PD [20,21]. Therefore, it is reasonable to hypothesize that impairments to the autophagy pathway may be causative for disease, although

the late age of onset in PD patients suggests that there are likely to be additional disease drivers or modifiers that involves the slow accumulation of damage over time.

Here, we report the changes in autophagy cargo observed using unbiased proteomics to analyze two distinct mouse models of PD, *PINK1* knock-out mice and *LRRK2*^{G2019S} knock-in mice. In both models, we find evidence for the upregulation of compensatory pathways for protein clearance and organelle quality control. PINK1 loss in mice leads to compensatory changes in autophagy machinery, so that mitochondria are still engulfed within autophagic vesicles (AVs). In LRRK2^{G2019S} mice, we find evidence of increased secretion, which may help to maintain neuronal homeostasis by removal of damaged organelles or aggregated proteins from the affected neurons. Further, we analyze how the AV cargo changes with age, finding that age-associated changes to lysophagy are distinct from the changes seen in genetic PD models, but may further exacerbate disease progression. Overall, we report many changes to autophagy in PD-associated models and highlight a common theme of compensation in response to PD-associated mutations to maintain the clearance of neuronal proteins.

RESULTS

Autophagic vesicles from PINK$^{-/-}$ mice contain mitochondria

PINK1 is a kinase that stabilizes and amplifies ubiquitination on damaged mitochondria to promote autophagosome formation and clearance [5]. However, previous studies in Drosophila and mouse indicate that under basal conditions, PINK1 and/or Parkin contribute minimally to mitochondrial turnover [12,17,22]. Therefore, we were curious to define the broader impacts of PINK1 loss on overall mitochondrial turnover by autophagy.

We investigated the autophagic cargo in brains collected from 7-month-old PINK1$^{-/-}$ mice compared to aged matched wild type mice. We previously confirmed that AV enrichment yields preparations in which ≥85% of vesicles were bona fide AVs. To assess the likelihood that a given protein in our AV fraction is a true cargo destined for degradation, we calculated a parameter termed the "cargo score" by determining its enrichment in a proteinase K-protected fraction relative to the total AV fraction[17].

Over 600 proteins exhibit significantly different cargo scores in AVs derived from PINK1$^{-/-}$ brains as compared to scores determined for AVs isolated from the brain of age-matched wild-type mice, indicative of widespread alterations in protein and organelle turnover (Figure 1a, Supplementary Table 1). Gene ontology (GO) analysis on the proteins that exhibited significantly decreased cargo scores from PINK1$^{-/-}$ brain as compared to WT suggests that certain mitochondrial proteins have decreased engulfment under basal conditions (Figure 1b).

To further understand how the observed changes in cargo are reflective of the state of the brain, we immunoblotted for proteins of interest from total brain and AV fractions. Increased enrichment of the protein within the AV could reflect higher levels of total protein in the brain, or alternatively indicate higher rates of turnover via autophagy. Therefore, we first compared levels in brain lysates between WT and PINK1$^{-/-}$, and then compared the levels of the proteins in the AV and AV+PK fraction between WT and PINK1$^{-/-}$. 34/82 of the mitochondrial proteins that are lower in PINK1$^{-/-}$ AVs are mitochondrial transcription and translation associated (Supplementary Table 2), suggesting there is a loss of autophagic engulfment of this specific subset of mitochondrial proteins in PINK1$^{-/-}$ mice. We confirmed these observations by focusing on GFM2, a mitochondrial elongation factor responsible for ribosome release during translation that had one of the highest fold changes between WT and PINK1$^{-/-}$ cargo scores. While GFM2 levels are not altered in brain

lysates of PINK1$^{-/-}$ mice relative to wild type mice, we noted that this protein is significantly decreased within PINK1$^{-/-}$ derived AVs (Figure 1c). EM analysis of enriched autophagosomes from wild type and PINK1$^{-/-}$ mouse brains shows that there is a slight, but significant decrease in the fraction of AVs that contain mitochondrial fragments, although there is no difference in acidified vesicles, or vesicles that contain synaptic vesicle like structures (Figure 1g, h, Supplementary Figure 1a,b). However, still 30% of the AVs derived from the PINK1$^{-/-}$ mice contain mitochondrial fragments.

Our previous work highlighted a surprising enrichment of mitochondrial nucleoids within brain AVs, and showed that TFAM-positive nucleoids are engulfed constitutively within the axon in primary neurons [17]. TFAM is also enriched within autophagosomes isolated from the brain of PINK1$^{-/-}$ knockout mice. However, total TFAM levels in PINK1$^{-/-}$ brain lysates were significantly lower than levels seen in wild type brain lysates (Figure 1i-l). Therefore, comparing the amount of TFAM within AVs relative to the total amount in the brain, AVs are engulfing proportionally more TFAM in PINK1$^{-/-}$ mice (Figure 1m). qPCR analysis did not detect changes in the amount of mtDNA present in whole brain samples from WT compared to PINK1$^{-/-}$ mice (Supplementary Figure 1c), thus further investigation on the impact of decreased TFAM levels following the loss of PINK1 in total brain is required.

PINK1$^{-/-}$ mice increase selective autophagic pathways to remove mitochondria

The continued clearance of mitochondrial fragments and TFAM-positive nucleoids in PINK1$^{-/-}$ derived AVs led us to ask whether we might find evidence for compensatory changes in autophagy in this PD model. Such compensatory changes might explain the limited phenotypic consequences observed in knock-out mice despite the loss of an important quality control pathway. Indeed, proteins associated with selective mitophagy had increased likelihood to be AV cargo in the absence of PINK1 (Figure 2a,b). FIS1 was found at increased levels in the AVs from PINK1$^{-/-}$ brains, while MFF levels were unchanged (Figure 2c-f, Supplementary Figure 2a-d). As FIS1 is associated with the fission of damaged mitochondrial components, and MFF is associated with mitochondrial maintenance and biogenesis [23], this suggests that damaged mitochondria are still effectively cleared in PINK1$^{-/-}$ mice.

Thus, we examined alternate pathways for the selective removal of damaged mitochondria. We observed increased BNIP3[24,25] and BCL2L13[26,27], two previously reported mitophagy receptors, in AVs from PINK1$^{-/-}$ brains by mass spectrometry (Figure 2a). We compared these two adaptors in whole brain and AV fractions by immunoblot (Figure 2g-n) and found higher levels of BCL2L13 in PINK1$^{-/-}$ total brain lysate relative to wildtype (Figure 2l). Both BNIP3 and BCL2L13 were enriched in AVs from PINK1$^{-/-}$ mice, suggesting that these mitophagy receptors may be preferentially engaged to compensate for the loss of PINK1 (Figure 2j, n). HUWE1, an E3 ligase that regulates PINK1$^{-/-}$ independent mitophagy by ubiquitylating MFN2 and recruiting AMBRA1 to initiate autophagosome formation [28], was identified as significantly increased in PINK1$^{-/-}$ brain derived AVs by proteomics (Figure 2a). Although immunoblot analysis did not show changes to HUWE1 (Supplementary Figure 2f-i), we did note increased engulfment of MFN2 in AVs (Figure 2o-r), suggesting this pathway may be activated to recruit mitochondria to autophagosomes. Together, the changes suggest evidence of upregulation of compensatory pathways to remove damaged mitochondria in the absence of PINK1.

We also noted changes to synaptic proteins, another major cargo of basal autophagy, within the PINK1$^{-/-}$ brain AVs (Supplementary Figure 3a). Proteomics suggests that the autophagic engulfment of both pre- and post-synaptic density proteins were significantly changed in PINK1$^{-/-}$ brain-derived AVs as compared to wild type (Supplementary Figure 3a,b). The multiple

statistically significant changes observed by MS are consistent with the observed broad changes in synapse formation and dendritic morphology induced by the loss of PINK1 [29–31]. Close inspection of the proteomic dataset also identified significant differences in proteins in the nitric oxide (NO) and spermidine synthesis pathway in the PINK1$^{-/-}$ brain-derived AVs (Supplementary Figure 3c). We immunoblotted for NOS1, SRM, and MAT2A, proteins required for NO and spermidine synthesis, in WT and PINK1$^{-/-}$ total brain and brain-derived AVs (Supplementary Figure 3d-o), and found that there are higher levels of these proteins in brains of PINK1$^{-/-}$ mice, suggesting possible increased production of NO and spermidine in PINK1$^{-/-}$ mouse brain. Supplemental spermidine rescues growth phenotypes in mitophagy deficient yeast [32], and increases WIPI2 levels, a protein that promotes autophagosome biogenesis in neurons[33], and autophagic flux in aged hippocampal neurons [34]. Consistent with these findings and the idea that spermidine production may be increased, immunoblotting indicated that total brain levels of WIPI2 were also increased (Supplementary Figure 3p-s).

LRRK2^{G2019S} alters the autophagy of proteins regulating extracellular vesicle production

Mutations in the *LRRK2* gene are the most common familial cause of PD, resulting in hyperactive LRRK2 kinase activity. Evidence of elevated LRRK2 kinase activity has also been shown in idiopathic PD cases [35]. Hyperactive LRRK2 increases the phosphorylation of RAB proteins that regulate vesicular trafficking [14,36]. Previously, we have shown that the G2019S mutation in LRRK2 leads to significant impairment in the trafficking and acidification of AVs [16]. Thus, we were curious how autophagic cargos might be altered in the brains of LRRK2^{G2019S} mice, and how these alterations might compare to the changes observed in PINK1$^{-/-}$ mice.

Overall, 71 proteins exhibited significantly different cargo scores when comparing results from analysis of brain-derived AVs from LRRK2^{G2019S} and wild type mice (Figure 3a, Supplementary Table 3), an order of magnitude less than the observed 652 proteins with significantly different cargo scores found in comparisons of PINK1$^{-/-}$ and wild type derived AVs. Yet 73% of the significant LRRK2^{G2019S} changes were common to the changes observed in the PINK1$^{-/-}$ model, identifying some similar response (Supplementary Figure 4 a,b). Autophagy cargo decreased in both PINK1$^{-/-}$ and LRRK2^{G2019S} brain as compared to wild type include synapse-related proteins (Supplementary Table 4), suggesting that some remodeling of synapses is common to different forms of PD. While we observed a mild reduction in the fraction of PINK1$^{-/-}$ derived AVs containing mitochondrial fragments, expression of LRRK2^{G2019S} did not affect the number of AVs with mitochondrial cargo (Supplementary Figure 4 c,d).

Most strikingly, GO analysis of the significantly changed AV cargo proteins from LRRK2^{G2019S} brains found that terms for extracellular organelles were enriched, including a lower cargo score for TSG101 and a higher cargo score for PIKFYVE (Figure 3a, b). Immunoblotting confirmed that TSG101, involved in the formation of extracellular vesicles (EVs) and commonly used as a marker of EVs [37], was decreased in LRRK2^{G2019S} AVs (Figure 3c-f). PIKFYVE is a kinase that phosphorylates PI3P to PI(3,5)P2, thereby regulating vesicular dynamics, lysosome fission and the fusion of multivesicular bodies to the lysosome [38–40]. When PIKFYVE is inhibited, it results in increased EV release [41,42]. Immunoblotting identified lower, although non-significant, levels of PIKFYVE in LRRK2^{G2019S} brain (Figure 3g, h). While AV levels of PIKFYVE were lower, the amount protected from proteinase K was sustained (Figure 3i-k). This suggests that the lower levels of PIKFYVE in the brain may result from autophagic degradation.

Based on these results, we wondered if the secretion of EVs was increased in the LRRK2 model. Consistent with this possibility, we found increased levels of TSG101 in conditioned media from LRRK2^{G2019S} primary cortical neurons, which could be reduced by kinase inhibition of LRRK2 with

MLi2 (Figure 3l, m, Supplementary Figure 4e, f). Additionally, proteomics identified increased levels of hnRNPK within AVs in LRRK2^{G2019S} (Figure 3a), which has been previously shown to be secreted in EVs in an autophagy-dependent manner [43]. Although changes in hnRNPK levels within AVs from LRRK2^{G2019S} did not reach statistical significance by immunoblotting (Supplementary Figure 4i-l), levels of hnRNPK in conditioned media were elevated in a kinase-dependent manner, as inhibition of LRRK2 kinase activity by MLi2 reduced the amount of hnRNPK secreted (Figure 3n, o, Supplementary Figure 4g, h). Together, these data suggest that while uptake into autophagosomes is not profoundly affected in the LRRK2 model, there are changes consistent with an induction of secretory autophagy to maintain proteostasis upon inhibition of lysosomal degradation, as discussed by Solvik et al.[44].

Aging leads to decreased lysosomal cargo in AVs

Aging is the most significant risk factor for PD, common to both familial and sporadic cases. Thus, we next asked whether aging can affect the nature of cargo turned over by autophagy in the brain, and if this might also contribute to PD progression. We proteomically profiled AVs derived from the brains of young (1-month-old) and old (18-month-old) mice for comparison of age-dependent changes [45].

Overall, 94 proteins were observed to significantly change with aging in AVs isolated from young and old mouse brains (Figure 4a, Supplementary Table 5). Only two of the proteins, PSMB4 and EDIL3, overlapped with changes found in LRRK2^{G2019S} brains (Supplementary Figure 5a). 27 proteins overlapped with changes found in PINK1$^{-/-}$ brains (Supplementary Figure 5 b,c). GO analysis on the cargo scores significantly lower in old mice indicates that engulfment of lysosomal proteins is decreased (Figure 4b). Immunoblotting confirmed two proteomic hits, GLA and SCARB2 decrease in AVs with age (Figure 4c-j). We further investigated other lysosomal membrane proteins LAMP1 and RagA and found that these too were decreased in the AV+PK fractions from old mice (Supplementary Figure 5 d-k).

We hypothesize that decreased lysophagy, as opposed to decreased autophagosome acidification, was responsible for the lower levels of lysosomal proteins in AVs derived from aged mice for three reasons. The lysosomal membrane proteins LAMP1 and RagA are found within the proteinase K protected fraction in AVs from young mice, whereas if autophagosome-lysosome fusion was impaired, membrane proteins should remain on the surface of the autophagolysosome (APL) and thus be degraded by the addition of protease (Supplementary Figure 5g, k). Additionally, EM analysis between AVs derived from young and old mouse brain does not indicate a change in the number of APLs, identified by dense, unilamellar structures (Supplementary Figure 5m, n). Lastly, there is no delay in the rate of autophagosome acidification with age in dorsal root ganglion neurons (DRGs) [46]. To confirm whether lysophagy could be affected with age, we investigated whether LGALS8, a crucial component of lysophagy [47],or the lysophagy receptors p62/SQSTM1 and TAX1BP1 [9,10] changed in total brain and in AVs with age. We found that the amount of LGALS8 and p62/SQSTM1 in the total brain lysate decreased, while total brain levels of TAX1BP1 were strongly increased, suggesting there may be an impairment in lysophagy in aging brain (Figure 4k-v).

Increased autophagic engulfment of α-synuclein with age

GO analysis of the cargos significantly enriched in AVs isolated from old mice compared to young mice include terms related to mitochondria and synapses (Figure 5a, b), similar to our findings from AVs isolated from 7-month-old mice [17]. EM of enriched autophagosomes did not show any

obvious changes to the mitochondrial cargo, as mitochondrial fragments were identified in about half of the AVs examined (Supplementary Figure 5m, o).

We noted the higher levels of α- and β- synuclein in AVs isolated from the brains of older mice (Figure 5a). α-synuclein is known to be degraded by autophagy [20,48] and is a key component of Lewy bodies that correlate with PD progression [49]. We confirmed that α-synuclein levels increased within AVs with age by immunoblotting (Figure 5c-f). We did not find changes in the amount of fibrillar proteins by Thioflavin T staining in total brain or within AVs with age, nor changes to phosphorylated α-synuclein (Supplementary Figure 6a-d). We further validated an increased colocalization of endogenous α-synuclein with endogenous LC3 puncta by immunocytochemistry in the cell body of dorsal root ganglion neurons from 18-month-old compared to 1-month-old mice (Figure 5g-f). Immunostaining indicated that colocalization of the lysosomal protein LAMP1 with LC3 is maintained (Figure 5j, k). We did not observe any changes to the colocalization of α-synuclein with LAMP1 with age, consistent with our analysis that the α-synuclein in AVs is monomeric (Figure 5l, m).

Secretion of α-synuclein is increased in LRRK2 mice

α-synuclein pathology spreads in PD patient brains in a stereotypical pattern that correlates with the staging of clinical symptoms. Previous research has demonstrated that exogenous α-synuclein fibrils can induce Lewy body formation in neurons both in vitro and in mouse brain via a prion-like activity [50–56]. We investigated whether the LRRK2^{G2019S} mutation affected AV levels and the extracellular release of α-synuclein. Levels of α-synuclein within AVs were unchanged in the adult LRRK2^{G2019S} brain-derived AVs (Figure 6a-c, Supplementary Figure 7a). However, the hyperactive kinase activity of LRRK2^{G2019S} in primary cortical neurons resulted in increased secretion of α-synuclein into the conditioned media, as these elevated levels can be rescued by treatment with MLi2 (Figure 6d-f).

We next investigated whether the increased secretion of α-synuclein from LRRK2^{G2019S} neurons correlated with changes to the circulating plasma levels in mice, and whether increasing age might also increase secretion. We confirmed that the levels of α-synuclein within AVs increased with age, but were unaffected by the LRRK2^{G2019S} mutation (Figure 6g-i). We observed an increase in plasma levels of α-synuclein in the LRRK2^{G20191S} mutant mice consistent with the increased levels in conditioned media from primary neurons, but surprisingly we did not observe any further change in the plasma levels of α-synuclein with age (Figure 6j).

We investigated whether TSG101 levels were changing within AVs or in plasma with age and the LRRK2 mutation. As observed previously, TSG101 levels associated with AVs were decreased with the LRRK2 mutation, but we did not observe further changes to the levels in AVs with age (Figure 6k-m, Supplementary Figure 7a). TSG101 levels in plasma increased with the LRRK2^{G2019S} mutation, but was not further increased with age (Figure 6n), which tracks with the same pattern of secreted α-synuclein.

We compared the AV levels, extracellular secreted and plasma levels of TFAM from adult and aged wild type and LRRK2^{G2019S} mice and embryonic primary cortical neurons (Figure 6o-r, Supplementary Figure 7b,c). TFAM levels within brain-derived AVs decreased with the LRRK2^{G2019S} and age (Figure 6q), and levels of secretion of TFAM into conditioned media from LRRK2^{G2019S} primary cortical neurons were not significantly increased (Supplementary Figure 7b,c). However, we detected higher plasma levels of TFAM in LRRK2^{G2019S} mice that further increased with age (Figure 6r). These data suggest there are multiple pathways of secretion that

are upregulated in LRRK2^{G2019S} mice, one for TSG101-positive EVs that is LRRK2 kinase dependent, and another for mitochondrial fragments or mtDNA.

DISCUSSION

We identify distinct degradative signatures in mouse models of PD, characterized by changes to cargos turned over by basal autophagy in the brain. These changes in autophagosome cargo are reflective of overall changes to neuronal biology, including alterations in synaptic protein turnover in PD[57] and changes to the lysosome in aged brain[58]. We find evidence for activation of compensatory mechanisms to maintain protein and organelle clearance, including increased autophagosome biogenesis and mitophagy adaptors in the absence of PINK1, and increased secretion in LRRK2^{G2019S} brain. We propose that these compensatory pathways maintain neuron health in the short term. However with age and further age-related stresses, there may be repercussions to the engagement of compensatory mechanisms that may ultimately contribute to PD onset, such as increased secretion leading to cell-to-cell transfer of α-synuclein or the inflammatory molecule mtDNA.

We find increased expression and use of alternative mitophagy adaptors in PINK1$^{-/-}$ mice (Figure 2). We have not directly tested whether the compensatory mitophagy pathways are as efficient as PINK1/Parkin at clearing damaged mitochondria, but because we observed fewer AVs containing mitochondrial fragments (Figure 1h), and PINK$^{-/-}$ mouse models are reported to have increased mitochondrial dysfunction with age or with mitochondrial damage[59,60], we suspect that the adaptive mechanisms are less resistant to additional stresses. We hypothesize that a there may also be an increase in autophagosome biogenesis in PINK1$^{-/-}$ mice because of the increase in WIPI2 levels (Supplementary Figure 3q) as reported in Maglione et al., 2019, although further in vitro flux assays are required to confirm. We believe that the higher levels of alternate mitophagy adaptors, potentially in combination with increased autophagic flux, may be responsible for the lower levels of TFAM observed in the PINK1$^{-/-}$ brain. We do not yet know how this impacts mitochondrial function or resilience, considering that mtDNA levels appear unaffected in total brain lysates. Additionally, we propose that the adaptations implemented may contribute to the abnormal development of synapses observed in PINK1 deficient animals and primary neurons [29–31,61]. Previously, abnormal synapses following PINK1 loss were attributed to reduced bioenergetic capacity, based on the relocalization of mitochondria to active post-synapses [62]. We propose that abnormal NO production predicted based on the higher levels of NOS1 in PINK1$^{-/-}$ mouse brain tissue (Supplementary Figure 3e), coupled with the observed changes in synapse proteins within the AVs from PINK1$^{-/-}$ mice (Supplementary Figure 3a,b), may contribute to the observed synapse remodeling described in PINK1$^{-/-}$ mice and neurons [63]. These changes are likely specific to certain proteins however, as we did not observe any changes in the fraction of AVs containing synaptic vesicle-like structures (Supplementary Figure 1a).

AVs derived from LRRK2^{G2019S} mouse brain displayed fewer significant changes to the AV cargo, but our analysis indicated that secretion was upregulated (Figure 3a). Impaired autophagosome-lysosome fusion increases the secretion of autophagosome cargo [41,44]. Therefore, we hypothesize that the defect in trafficking and acidification caused by LRRK2^{G2019S} [16] results in an increase in secretion of some of the AV cargo through EVs as a compensatory mechanism to remove undegraded cargo. Autophagosomes can fuse with MVBs to form amphisomes, which can then release EVs extracellularly [64–66], or autophagy cargo can be directly loaded into MVBs in an LC3-dependent mechanism [43], but we cannot yet determine if one of these pathways drives the observed compensation more than the other. Interestingly, we identified several biomarkers of neurodegenerative disease as changed within the AVs from LRRK2^{G2019S} mouse brains

(Supplementary Table 3). Other autophagy cargo may provide candidates for novel biomarkers to detect changes to autophagy before later stages of disease progression.

We find that with advanced age, we see fewer lysosomal proteins and more α-synuclein as AV cargo (Figure 4, Figure 5). Cell biology and GWAS studies strongly implicate lysosomal failure as causative for PD pathology [67] , therefore impaired clearance of damaged lysosomes with age may be a contributing factor, and further exacerbate disease progression. We predict that lower levels of LGALS8 and p62/SQSTM1 contribute to the decrease in lysosomal proteins present in AVs derived from older mice, and the accumulation of TAX1BP1 is reflective of the impairments of lysosome degradation by autophagy. α-synuclein pre-formed fibrils are rapidly endocytosed and delivered to the lysosome and can induce lysosomal rupture [68], which may contribute to the seeding progression of α-synuclein aggregates [69]. We suspect that increased delivery of α-synuclein to the lysosome with age may result in more damaged lysosomes that require lysophagy. If the observed decreases in LGALS8 decrease the rate of lysophagy with age, the increase in α-synuclein in AVs may further aggravate the accumulation of defective lysosomes.

Increased secretion of α-synuclein in the LRRK2^{G2019S} primary cortical neurons and mice is consistent with previous findings linking both impaired autophagy and the LRRK2^{G2019S} mutation to increased secretion of α-synuclein [70–72]. We believe that in addition to increased phosphorylation of Rab35, the impaired acidification of autophagosomes in the LRRK2^{G2019S} model [16] results in the unconventional secretion of α-synuclein, similar to the secretion of α-synuclein and autophagosome cargo via Rab27a mediated pathways [44,70]. Both Rab27a and Rab35 have been linked to exosome secretion, consistent with our findings of higher TSG101 secretion in the LRRK2^{G2019S} mice in the same pattern as α-synuclein secretion (Figure 3m, Figure 6e, j, n).

In a surprising finding, although the levels of α-synuclein increase within AVs with age, this does not correlate with the plasma levels of α-synuclein in aged LRRK2^{G2019S} mice (Figure 6j), which we would expect from a model where AVs fuse directly with MVBs, and the inner AV membrane becomes the EV itself. We cannot yet rule out that the amount of α-synuclein secreted by aged neurons is unchanged, as clearance by surrounding glia may affect the amount of α-synuclein that ends up in the plasma. However, assuming that the plasma levels are indeed reflective of the amount secreted from neurons, there are a few alternative models that fit the data. Recent research has demonstrated that α-synuclein aggregates can be released extracellularly from the lysosome or acidified MVBs [73,74]. If α-synuclein pre-formed fibril transfer occurs primarily on the surface of exosomes following the fusion of lysosomes to multivesicular bodies as proposed in Bayati et al., 2022, the number of EVs secreted may be the limiting factor for the amount of secreted α-synuclein in aged LRRK2^{G2019S} mice. As acidification of the AVs does not decrease with age [46], we would not expect increases to EV secretion with age as found in the LRRK2^{G2019S} mice, which is supported by our measurements of the plasma levels of TSG101 in aged mice (Figure 6n).

The distinct pattern of secretion of TFAM that is increased in both LRRK2^{G2019S} and aged mice (Figure 6r) suggests an alternative pathway of secretion compared to α-synuclein. Recently, damaged mitochondria were shown to be secreted in an autophagy dependent manner distinct from the secretion of small EVs when normal autophagy is inhibited in ATG7$^{-/-}$ cells [75]. Our findings are consistent with these results, but we cannot yet determine what is driving the increased extracellular levels of TFAM. We posit that alternative secretion of TFAM in aging and the LRRK2 mutation may contribute to inflammation that drives PD progression, as TFAM is associated with mtDNA, which is potently pro-inflammatory when released from the mitochondria [76,77].

Is compensatory secretion in the context of impaired autophagy good or bad for neuron health? Most likely it is both, depending on context. We found that the α-synuclein in AVs from WT brain did not seem to be aggregated or fibrillar (Supplementary Figure 6). If LRRK2 mutations cause monomeric α-synuclein secretion as we suggest, it may prevent intra-neuronal buildup that can promote pathogenic aggregation, and the secreted α-synuclein may be cleared extracellularly by microglia [78]. Indeed, decreased α-synuclein in the CSF is correlated with PD-diagnosis and further reduced with older age, suggesting that secretion is protective to remove α-synuclein from the neuron where it may aggregate [18]. However if the α-synuclein is aggregated prior to secretion, as is the case with pre-formed fibrils, secretion in response to impaired autophagy could propagate PD pathology and accelerate disease progression as previously found [79,80]. If aging results in increased α-synuclein delivery to the lysosome and MVB that outpaces its secretion on the surface of EVs, could this further contribute to aggregation and Lewy body formation?

Although both genetic PD models upregulate pathways to compensate for impaired autophagy, each response is specific to the type of autophagy impairment. It would not be beneficial to increase autophagosome formation in the LRRK2^{G2019S} model via the same process as in the PINK1$^{-/-}$ model if the extra autophagosomes will only then get stuck in a traffic jam. How the different impairments to autophagy are sensed and subsequently compensated for is a question that requires further study, as it may identify targetable avenues for novel PD therapies. In all, our proteomic analysis identifies changes to the autophagy pathway that may contribute to PD progression in multiple ways, including regulating Lewy body propagation, neuroinflammation and mitochondrial and synapse dysfunction, further cementing the crucial role of autophagy in maintaining neuron health and demonstrating the importance of this pathway in neurodegenerative disease progression.

Acknowledgments

We thank Mariko Tokito for assistance in the cloning of plasmid constructs, Karen Wallace Jahn for assistance with animal models, and J.A. Paulo for proteomics support. This research was supported by the German Research Foundation (DFG; BO 5434/2-1 to C.A.B.), by the National Institutes of Health grant NS083524 (JWH) and by Sloan Kettering Institute startup funds (AO). The study is funded by the joint efforts of The Michael J. Fox Foundation for Parkinson's Research (MJFF) and the Aligning Science Across Parkinson's (ASAP) initiative. MJFF administers the grants ASAP-000350 (ELFH), ASAP-000282 (JWH) on behalf of ASAP and itself.

Author Contributions

JG, ELFH and JWH, project design and conceptualization; JG and ELFH, co-writing – original draft; JG, ELFH, JWH, CAB, AKHS and AO, editing manuscript; AKHS, DRG isolation, culture and fixation; CAB, primary cortical neuron isolation, culture and sample collection; MA, IB assistance; AO, proteomics data collection and analysis; JG, resources, data collection, data analysis and interpretation; ELFH, JWH funding acquisition.

Declaration of Interests

JWH is a co-founder and advisory board member of Caraway Therapeutics, and is a founding scientific advisory board member for Interline Therapeutics.

Inclusion and Diversity

We worked to ensure sex balance in the selection of rodent subjects. While citing references scientifically relevant for this work, we also actively worked to promote gender balance in our reference list.

Figure 1: PINK1$^{-/-}$ derived AVs maintain mitochondrial fragments as cargo at a diminished level

a. Volcano plot analysis of the ratio of AV+PK to AV derived from brain of PINK1$^{-/-}$ relative to WT mice. Significantly increased or decreased proteins are depicted as larger circles. WT n=6; PINK1$^{-/-}$ n=6. Proteins annotated as mitochondrial using the MitoCarta3 database are denoted in green. **b.** Graph of p-values of the top gene ontology terms using the Enrichr database from proteins significantly lower in PINK1$^{-/-}$ derived AVs (the dotted box in panel a.) **c-f.** Representative immunoblot (**c**) and quantifications (mean ± SEM, unpaired t test) of the levels of GFM2 in total brain (**d**), AV fraction (**e**), and AV+PK fraction (**f**), normalized to total protein and WT total brain lysate levels. WT n=4, PINK1$^{-/-}$ n=5. **g.** Representative electron micrographs of AVs derived from WT and PINK1$^{-/-}$ mouse brains. Insert highlights an identified AV containing a mitochondrial fragment and synaptic vesicle like structures. **h.** Quantification of AVs containing mitochondria from EM images (WT n=3; PINK1$^{-/-}$ n=3, >400 events counted per biological replicate). **i-m.** Representative immunoblot (**i**) and quantifications (mean ± SEM, unpaired t test) of the levels of TFAM in total brain (**j**), AV fraction (**k**), and AV+PK fraction (**l**), normalized to total protein and WT total brain lysate levels, or (**m**) AV+PK fraction normalized to total protein and internally normalized to total brain levels. WT n=5, PINK1$^{-/-}$ n=6.

Figure 2: PINK1$^{-/-}$ mice upregulate and rely on alternate mitophagy receptors

a. Identical volcano plot analysis as in Figure 1a, with alternate mitophagy receptors highlighted in orange. **b.** Schematic of alternative mitophagy adaptors. **c-f.** Representative immunoblot (**c**) and quantifications (mean ± SEM, unpaired t test) of the levels of FIS1 in total brain (**d**), AV fraction (**e**), and AV+PK fraction (**f**), normalized to total protein and WT total brain lysate levels. WT n=5, PINK1$^{-/-}$ n=6. **g-j.** Representative immunoblot (**g**) and quantifications (mean ± SEM, unpaired t test) of the levels of BNIP3 in total brain (**h**), AV fraction (**i**), and AV+PK fraction (**j**), normalized to total protein and WT total brain lysate levels. WT n=4, PINK1$^{-/-}$ n=4. **k-n.** Representative immunoblot (**k**) and quantifications (mean ± SEM, unpaired t test) of the levels of BCL2L13 in total brain (**l**), AV fraction (**m**), and AV+PK fraction (**n**), normalized to total protein and WT total brain lysate levels. WT n=4, PINK1$^{-/-}$ n=6. **o-r.** Representative immunoblot (**o**) and quantifications (mean ± SEM, unpaired t test) of the levels of MFN2 in total brain (**p**), AV fraction (**q**), and AV+PK fraction (**r**), normalized to total protein and WT total brain lysate levels. WT n=4, PINK1$^{-/-}$ n=5.

Figure 3: LRRK2^{G2019S} mice increase secretion of EVs

Volcano plot analysis of the ratio of AV+PK to AV derived from brain of LRRK2^{G2019S} relative to WT mice. Significantly increased or decreased proteins are depicted as larger circles, except ALIX which is highlighted but did not meet the defined statistical cut-off. WT n=6; LRRK2^{G2019S} n=5. Proteins reported to be EV cargo are highlighted in aqua. Proteins involved in EV formation and a validated EV cargo hnRNPK are highlighted in teal. **b.** Graph of p-values of the top gene ontology terms using the Enrichr database of all proteins significantly changed within AVs (the dotted box in panel a.) **c-f.** Representative immunoblot (**c**) and quantifications (mean ± SEM, unpaired t test) of the levels of TSG101 in total brain (**d**), AV fraction (**e**), and AV+PK fraction (**f**), normalized to total protein and WT total brain lysate levels. WT n=4, LRRK2^{G2019S} n=4. **g-k.** Representative immunoblot (**g**) and quantifications (mean ± SEM, unpaired t test) of the levels of PIKFYVE in in total brain (**h**), AV fraction (**i**), and AV+PK fraction (**j**), normalized to total protein and WT total brain lysate levels, or (**k**) levels of AV+PK normalized to total protein and AV levels. WT n=4, LRRK2^{G2019S} n=4. **l-m.** Immunoblot (**l**) and (**m**) quantification (mean ± SEM, ANOVA with Šídák's) of levels of TSG101 in conditioned media from WT or LRRK2^{G2019S} primary cortical neurons, treated with DMSO or the LRRK2 kinase inhibitor MLi2 (100nM for 72h), normalized to total protein levels and WT, DMSO control. n=3 per condition. **n-o.**

Representative immunoblot (**n**) and (**o**) quantification (mean ± SEM, ANOVA with Šídák's) of levels of hnRNPK in conditioned media from WT or LRRK2^{G2019S} primary cortical neurons, treated with DMSO or MLi2 (100nM for 72h), normalized to total protein levels and WT, DMSO control. n=3 per condition.

Figure 4: Evidence of decreased lysophagy in the brain with age

a. Volcano plot analysis of the ratio of AV+PK to AV derived from brain of 18-month-old relative to 1-month-old WT mice. Significantly increased or decreased proteins are depicted as larger circles. 1-month n=10; 18-month n=11. Proteins annotated as lysosomal are denoted in purple. **b.** Graph of p-values of the top gene ontology terms using the Enrichr database from proteins significantly lower in old compared to young brain-derived AVs (the dotted box in panel a.) **c-f.** Representative immunoblot (**c**) and quantifications (mean ± SEM, unpaired t test) of the levels of GLA in total brain (**d**), AV fraction (**e**), and AV+PK fraction (**f**), normalized to total protein and WT total brain lysate levels. 1-month n=4, 18-month n=4. **g-j.** Representative immunoblot (**g**) and quantifications (mean ± SEM, unpaired t test) of the levels of SCARB2 in total brain (**h**), AV fraction (**i**), and AV+PK fraction (**j**), normalized to total protein and WT total brain lysate levels. 1-month n=3, 18-month n=3. **k-n.** Representative immunoblot (**k**) and quantifications (mean ± SEM, unpaired t test) of the levels of LGALS8 in total brain (**l**), AV fraction (**m**), and AV+PK fraction (**n**), normalized to total protein and 1-month total brain lysate levels. 1-month n=4, 18-month n=4. **o-r.** Representative immunoblot (**o**) and quantifications (mean ± SEM, unpaired t test) of the levels of p62/SQSTM1 in total brain (**p**), AV fraction (**q**), and AV+PK fraction (**r**), normalized to total protein and 1-month total brain lysate levels. 1-month n=4, 18-month n=4. **s-v.** Representative immunoblot (**s**) and quantifications (mean ± SEM, unpaired t test) of the levels of TAX1BP1 in total brain (**t**), AV fraction (**u**), and AV+PK fraction (**v**), normalized to total protein and 1-month total brain lysate levels. 1-month n=4, 18-month n=4.

Figure 5: α-synuclein is increased within AVs from older mice

a. Identical volcano plot analysis as in Figure 4a, with synapse associated proteins highlighted in maroon and mitochondrial proteins highlighted in green. α-synuclein and β-synuclein are annotated. **b.** Graph of p-values of the top gene ontology terms using the Enrichr database from proteins significantly higher in old compared to young brain-derived AVs (the dotted box in panel a.) **c-f.** Representative immunoblot (**c**) and quantifications (mean ± SEM, unpaired t test) of the levels of α-synuclein in total brain (**d**), AV fraction (**e**), and AV+PK fraction (**f**), normalized to total protein and 7-month old total brain lysate levels. 1-month n≥5, 18-month n≥5. **g.** Representative immunocytochemistry of DRGs derived from 1-month-old or 18-month-old mice, and co-stained for the lysosomal marker LAMP1, α-synuclein, and the autophagosome marker LC3. 1-month n=3, 18-month n=4. **h-m.** Quantification of ICC images (mean ± SEM, unpaired t test), separated by cell body and axon, using automated Mander's coefficient to quantify colocalization, as indicated in the y-axis labels.

Figure 6: α-synuclein, TSG101, and TFAM are increased in plasma of LRRK2^{G2019S} mice

a-c. Quantification (mean ± SEM, unpaired t test) of immunoblots for α-synuclein levels in LRRK2^{G2019S} relative to WT derived (**a**) total brain, (**b**) AV fraction, and (**c**) AV+PK fraction, normalized to total protein and WT total brain lysate levels. WT n=5, LRRK2^{G2019S} n=6. **d-e.** Representative immunoblot (**d**) and (**e**) quantification (mean ± SEM, ANOVA with Šídák's) of levels of α-synuclein in conditioned media from WT or LRRK2^{G2019S} primary cortical neurons, treated with DMSO or the LRRK2 kinase inhibitor MLi2 (100nM for 72h), normalized to total protein levels and WT, DMSO control. n=3 per condition. **f.** Quantification of levels of α-synuclein in WT or LRRK2^{G2019S} primary cortical neurons, treated with DMSO or the LRRK2 kinase inhibitor MLi2 (100nM for 72h), normalized to total protein levels and WT, DMSO control.

n=3 per condition. **g-i.** Quantifications of immunoblots (mean ± SEM, ANOVA with Šídák's) for the levels of α-synculein in total brain (**g**), AV fraction (**h**), and AV+PK fraction (**i**) from 7-month old and 18-month-old WT and LRRK2^{G2019S} mice, normalized to total protein and 7-month old WT total brain lysate levels. n=4 per condition. **j.** Quantification of immunoblots (mean ± SEM, ANOVA with Šídák's) for the level of α-synuclein from plasma from 7-month old and 18-month-old WT and LRRK2^{G2019S} mice, normalized to total protein and 7-month old WT plasma levels. n≥5 per condition. **k-m.** Quantifications of immunoblots (mean ± SEM, ANOVA with Šídák's) for the levels of TSG101 in total brain (**k**), AV fraction (**l**), and AV+PK fraction (**m**) from 7-month old and 18-month-old WT and LRRK2^{G2019S} mice, normalized to total protein and 7-month old WT total brain lysate levels. n≥3 per condition. **n.** Quantification of immunoblots (mean ± SEM, ANOVA with Šídák's) for the level of TSG101 from plasma from 7-month old and 18-month-old WT and LRRK2^{G2019S} mice, normalized to total protein and 7-month old WT plasma levels. n≥9 per condition. **o-q.** Quantifications of immunoblots (mean ± SEM, ANOVA with Šídák's) for the levels of TFAM in total brain (**o**), AV fraction (**p**), and AV+PK fraction (**q**) from 7-month old and 18-month-old WT and LRRK2^{G2019S} mice, normalized to total protein and 7-month old WT total brain lysate levels. n≥3 per condition. **n.** Quantification of immunoblots (mean ± SEM, ANOVA with Šídák's) for the level of TFAM from plasma from 7-month old and 18-month-old WT and LRRK2^{G2019S} mice, normalized to total protein and 7-month old WT plasma levels. n≥6 per condition.

References

1. Stavoe, A. K. H. & Holzbaur, E. L. F. Autophagy in Neurons. *Annu Rev Cell Dev Biol.* **35**, 477–500 (2019).
2. Wong, E. & Cuervo, A. M. Autophagy gone awry in neurodegenerative diseases. *Nat. Neurosci.* **13**, 805–11 (2010).
3. Fleming, A. & Rubinsztein, D. C. Autophagy in Neuronal Development and Plasticity. *Trends Neurosci.* **43**, 767–779 (2020).
4. Kirkin, V. & Rogov, V. V. A Diversity of Selective Autophagy Receptors Determines the Specificity of the Autophagy Pathway. *Mol. Cell* **76**, 268–285 (2019).
5. Lazarou, M. *et al.* The ubiquitin kinase PINK1 recruits autophagy receptors to induce mitophagy. *Nature* **524**, 309–314 (2015).
6. Wong, Y. C. & Holzbaur, E. L. F. Optineurin is an autophagy receptor for damaged mitochondria in parkin-mediated mitophagy that is disrupted by an ALS-linked mutation. *Proc. Natl. Acad. Sci. U. S. A.* **111**, E4439–E4448 (2014).
7. Ordureau, A. *et al.* Quantitative Proteomics Reveal a Feedforward Model for Mitochondrial PARKIN Translocation and Ubiquitin Chain Synthesis. *Mol. Cell* **56**, 462 (2014).
8. Heo, J.-M., Ordureau, A., Paulo, J. A., Rinehart, J. & Harper, J. W. The PINK1-PARKIN mitochondrial ubiquitylation pathway drives a program of TBK1 activation and recruitment of OPTN and NDP52 to promote mitophagy Jin-Mi. *Mol. Cell* **60**, 7–20 (2015).
9. Gallagher, E. R. & Holzbaur, E. L. F. The selective autophagy receptor p62 and the heat shock protein HSP27 facilitate lysophagy via the formation of phase-separated condensates. *bioRxiv* 1–49 (2022).
10. Eapen, V. V., Swarup, S., Hoyer, M. J., Paulo, J. A. & Harper, J. W. Quantitative proteomics reveals the selectivity of ubiquitin-binding autophagy receptors in the turnover of damaged lysosomes by lysophagy. *Elife* **10**, 1–36 (2021).
11. Hara, T. *et al.* Suppression of basal autophagy in neural cells causes neurodegenerative disease in mice. *Nature* **441**, 885–889 (2006).
12. McWilliams, T. G. *et al.* Basal Mitophagy Occurs Independently of PINK1 in Mouse Tissues of High Metabolic Demand. *Cell Metab.* **27**, 439-449.e5 (2018).
13. Maday, S., Wallace, K. E. & Holzbaur, E. L. F. Autophagosomes initiate distally and mature during transport toward the cell soma in primary neurons. *J. Cell Biol.* **196**, 407–417 (2012).
14. Steger, M. *et al.* Systematic proteomic analysis of LRRK2-mediated rab GTPase phosphorylation establishes a connection to ciliogenesis. *Elife* **6**, 1–22 (2017).
15. Homma, Y., Hiragi, S. & Fukuda, M. Rab family of small GTPases: an updated view on their regulation and functions. *FEBS J.* **288**, 36–55 (2021).
16. Boecker, C. A., Goldsmith, J., Dou, D., Cajka, G. G. & Holzbaur, E. L. F. Increased LRRK2 kinase activity alters neuronal autophagy by disrupting the axonal transport of autophagosomes. *Curr. Biol.* **31**, 2140-2154.e6 (2021).
17. Goldsmith, J., Ordureau, A., Harper, J. W. & Holzbaur, E. L. F. Brain-derived autophagosome profiling reveals the engulfment of nucleoid-enriched mitochondrial fragments by basal autophagy in neurons. *Neuron* 1–10 (2022) doi:10.1016/j.neuron.2021.12.029.
18. Pagano, G., Ferrara, N., Brooks, D. J. & Pavese, N. Age at onset and Parkinson disease phenotype. *Neurology* **86**, 1400–1407 (2016).
19. Anglade, P. *et al.* Apoptosis and autophagy in nigral neurons of patients with Parkinson's disease. *Histol. Histopathol.* **12**, 25–31 (1997).
20. Webb, J. L., Ravikumar, B., Atkins, J., Skepper, J. N. & Rubinsztein, D. C. α-synuclein Is Degraded by Both Autophagy and the Proteasome. *J. Biol. Chem.* **278**, 25009–25013

(2003).
21. Sato, S. *et al.* Loss of autophagy in dopaminergic neurons causes Lewy pathology and motor dysfunction in aged mice. *Sci. Rep.* **8**, 1–10 (2018).
22. Vincow, E. S. *et al.* Autophagy accounts for approximately one-third of mitochondrial protein turnover and is protein selective. *Autophagy* **15**, 1592–1605 (2019).
23. Kleele, T. *et al.* Distinct fission signatures predict mitochondrial degradation or biogenesis. *Nature* **593**, (2021).
24. Zhang, T. *et al.* BNIP3 protein suppresses PINK1 kinase proteolytic cleavage to promote mitophagy. *J. Biol. Chem.* **291**, 21616–21629 (2016).
25. Bellot, G. *et al.* Hypoxia-induced autophagy is mediated through hypoxia-inducible factor induction of BNIP3 and BNIP3L via their BH3 domains. *Mol. Cell. Biol.* **29**, 2570–81 (2009).
26. Otsu, K., Murakawa, T. & Yamaguchi, O. BCL2L13 is a mammalian homolog of the yeast mitophagy receptor Atg32. *Autophagy* **11**, 1932–1933 (2015).
27. Murakawa, T. *et al.* A Mammalian Mitophagy Receptor, Bcl2-L-13, Recruits the ULK1 Complex to Induce Mitophagy. *Cell Rep.* **26**, 338-345.e6 (2019).
28. Di Rita, A. *et al.* HUWE1 E3 ligase promotes PINK1/PARKIN-independent mitophagy by regulating AMBRA1 activation via IKKα. *Nat. Commun.* **9**, (2018).
29. Pearlstein, E., Michel, F. J., Save, L., Ferrari, D. C. & Hammond, C. Abnormal development of glutamatergic synapses afferent to dopaminergic neurons of the pink1–/– mouse model of Parkinson's disease. *Front. Cell. Neurosci.* **10**, 1–13 (2016).
30. Feligioni, M. *et al.* Subtle alterations of excitatory transmission are linked to presynaptic changes in the hippocampus of PINK1-deficient mice. *Synapse* **70**, 223–230 (2016).
31. Hernández, C. J., Báez-Becerra, C., Contreras-Zárate, M. J., Arboleda, H. & Arboleda, G. PINK1 Silencing Modifies Dendritic Spine Dynamics of Mouse Hippocampal Neurons. *J. Mol. Neurosci.* **69**, 570–579 (2019).
32. Kaur, J. *et al.* Atg32-dependent mitophagy sustains spermidine and nitric oxide required for heat-stress tolerance in Saccharomyces cerevisiae. *J. Cell Sci.* **134**, (2021).
33. Stavoe, A. K., Gopal, P. P., Gubas, A., Tooze, S. A. & Holzbaur, E. L. Expression of WIPI2B counteracts age-related decline in autophagosome biogenesis in neurons. *Elife* **8**, 1–36 (2019).
34. Maglione, M. *et al.* Spermidine protects from age-related synaptic alterations at hippocampal mossy fiber-CA3 synapses. *Sci. Rep.* **9**, 1–12 (2019).
35. Di Maio, R. *et al.* A central role for LRRK2 in idiopathic Parkinson Disease. *Sci. Transl. Med.* **451**, (2018).
36. Taylor, M. & Alessi, D. R. Advances in elucidating the function of leucine-rich repeat protein kinase-2 in normal cells and Parkinson's disease. *Curr. Opin. Cell Biol.* **63**, 102–113 (2020).
37. Kowal, J., Tkach, M. & Théry, C. Biogenesis and secretion of exosomes. *Curr. Opin. Cell Biol.* **29**, 116–125 (2014).
38. Assia, S. PIKfyve: partners, significance, debates and paradoxes. *Cell Biol Int.* **32(6)**, 591–604 (2008).
39. de Lartigue, J. *et al.* PIKfyve regulation of endosome-linked pathways. *Traffic* **10**, 883–893 (2009).
40. Sharma, G. *et al.* A family of PIKFYVE inhibitors with therapeutic potential against autophagy-dependent cancer cells disrupt multiple events in lysosome homeostasis. *Autophagy* **15**, 1694–1718 (2019).
41. Hessvik, N. P. *et al.* PIKfyve inhibition increases exosome release and induces secretory autophagy. *Cell. Mol. Life Sci.* **73**, 4717–4737 (2016).
42. Osborne, S. L. *et al.* PIKfyve negatively regulates exocytosis in neurosecretory cells. *J. Biol. Chem.* **283**, 2804–2813 (2008).

43. Leidal, A. M. *et al.* The LC3-conjugation machinery specifies the loading of RNA-binding proteins into extracellular vesicles. *Nat. Cell Biol.* **22**, (2020).
44. Solvik, T. A. *et al.* Secretory autophagy maintains proteostasis upon lysosome inhibition. *J. Cell Biol.* **221**, (2022).
45. Flurkey, K., Currer, J. M. & Harrison, D. E. Chapter 20 Mouse Models in Aging Research. *Mouse Biomed. Res.* 637–672 (2007).
46. Tsong, H., Holzbaur, E. & Stavoe, A. K. H. Aging Differentially Affects Axonal Autophagosome Formation and Maturation. *bioRxiv* 2022.08.27.505553 (2022).
47. Thurston, T. L. M., Wandel, M. P., Von Muhlinen, N., Foeglein, Á. & Randow, F. Galectin 8 targets damaged vesicles for autophagy to defend cells against bacterial invasion. *Nature* **482**, 414–418 (2012).
48. Friedman, L. G. *et al.* Disrupted autophagy leads to dopaminergic axon and dendrite degeneration and promotes presynaptic accumulation of alpha-synuclein and LRRK2 in the brain. *J. Neurosci.* **32**, 7585–7593 (2012).
49. Spillantini, M. G. *et al.* a -Synuclein in Lewy bodies. *Nature* **388**, 839–840 (1997).
50. Desplats, P. *et al.* Inclusion formation and neuronal cell death through neuron-to-neuron transmission of α-synuclein. *Proc. Natl. Acad. Sci. U. S. A.* **106**, 13010–13015 (2009).
51. Emmanouilidou, E. *et al.* Cell-produced α-synuclein is secreted in a calcium-dependent manner by exosomes and impacts neuronal survival. *J. Neurosci.* **30**, 6838–6851 (2010).
52. Nonaka, T., Watanabe, S. T., Iwatsubo, T. & Hasegawa, M. Seeded aggregation and toxicity of α-synuclein and tau: Cellular models of neurodegenerative diseases. *J. Biol. Chem.* **285**, 34885–34898 (2010).
53. Volpicelli-Daley, L. a *et al.* Exogenous α-synuclein fibrils induce Lewy body pathology leading to synaptic dysfunction and neuron death. *Neuron* **72**, 57–71 (2011).
54. Mougenot, A. L. *et al.* Prion-like acceleration of a synucleinopathy in a transgenic mouse model. *Neurobiol. Aging* **33**, 2225–2228 (2012).
55. Luk, K. C. *et al.* Pathological α-Synuclein Transmission Initiates Parkinson-like Neurodegeneration in Non-transgenic Mice. *Science (80-.).* **338**, 949–953 (2012).
56. Masuda-Suzukake, M. *et al.* Prion-like spreading of pathological α-synuclein in brain. *Brain* **136**, 1128–1138 (2013).
57. Soukup, S., Vanhauwaert, R. & Verstreken, P. Parkinson's disease: convergence on synaptic homeostasis. *EMBO J.* **37**, 1–16 (2018).
58. Nixon, R. A. The aging lysosome: an essential catalyst for late-onset neurodegenerative diseases. *Biochim. Biophys. Acta - Proteins Proteom.* **1868**, (2020).
59. Gautier, C. A., Kitada, T. & Shen, J. Loss of PINK1 causes mitochondrial functional defects and increased sensitivity to oxidative stress. *Proc. Natl. Acad. Sci. U. S. A.* **105**, 11364–11369 (2008).
60. Gispert, S. *et al.* Parkinson phenotype in aged PINK1-deficient mice is accompanied by progressive mitochondrial dysfunction in absence of neurodegeneration. *PLoS One* **4**, (2009).
61. Kitada, T. *et al.* Impaired dopamine release and synaptic plasticity in the striatum of PINK1-deficient mice. *Proc. Natl. Acad. Sci. U. S. A.* **104**, 11441–11446 (2007).
62. Li, Z., Okamoto, K. I., Hayashi, Y. & Sheng, M. The importance of dendritic mitochondria in the morphogenesis and plasticity of spines and synapses. *Cell* **119**, 873–887 (2004).
63. Richards, L. A. & Schonhoff, C. M. Nitric oxide and sex differences in dendritic branching and arborization. *J. Neurosci. Res.* **99**, 1390–1400 (2021).
64. Xu, J., Camfield, R. & Gorski, S. M. The interplay between exosomes and autophagy - partners in crime. *J. Cell Sci.* **131**, 1–11 (2018).
65. Gordon, P. B. & Seglen, P. O. Prelysosomal convergence of autophagic and endocytic pathways. *Biochem. Biophys. Res. Commun.* **151**, 40–47 (1988).
66. Berg, T. O., Fengsrud, M., Strømhaug, P. E., Berg, T. & Seglen, P. O. Isolation and

characterization of rat liver amphisomes: Evidence for fusion of autophagosomes with both early and late endosomes. *J. Biol. Chem.* **273**, 21883–21892 (1998).

67. Wallings, R. L., Humble, S. W., Ward, M. E. & Wade-Martins, R. Lysosomal Dysfunction at the Centre of Parkinson's Disease and Frontotemporal Dementia/Amyotrophic Lateral Sclerosis. *Trends Neurosci.* **42**, 899–912 (2019).
68. Freeman, D. *et al.* Alpha-Synuclein Induces Lysosomal Rupture and Cathepsin Dependent Reactive Oxygen Species Following Endocytosis. *PLoS One* **8**, (2013).
69. Jiang, P., Gan, M., Yen, S. H., McLean, P. J. & Dickson, D. W. Impaired endo-lysosomal membrane integrity accelerates the seeding progression of α-synuclein aggregates. *Sci. Rep.* **7**, 1–13 (2017).
70. Ejlerskov, P. *et al.* Tubulin polymerization-promoting protein (TPPP/p25α) promotes unconventional secretion of α-synuclein through exophagy by impairing autophagosome-lysosome fusion. *J. Biol. Chem.* **288**, 17313–17335 (2013).
71. Bae, E. J. *et al.* LRRK2 kinase regulates α-synuclein propagation via RAB35 phosphorylation. *Nat. Commun.* **9**, (2018).
72. Schapansky, J. *et al.* Familial knockin mutation of LRRK2 causes lysosomal dysfunction and accumulation of endogenous insoluble α- synuclein in neurons Jason. *Neurobiol. Dis.* **111**, 26–35 (2018).
73. Xie, Y. X. *et al.* Lysosomal exocytosis releases pathogenic α-synuclein species from neurons in synucleinopathy models. *Nat. Commun.* **13**, 4918 (2022).
74. Bayati, A. *et al.* Rapid macropinocytic transfer of α-synuclein to lysosomes. *Cell Rep.* **40**, 111102 (2022).
75. Tan, H. W. S. *et al.* A degradative to secretory autophagy switch mediates mitochondria clearance in the absence of the mATG8-conjugation machinery. *Nat. Commun.* **13**, 3720 (2022).
76. Sliter, D. A. *et al.* Parkin and PINK1 mitigate STING-induced inflammation. *Nature* **561**, 258–262 (2018).
77. Yu, C. H. *et al.* TDP-43 Triggers Mitochondrial DNA Release via mPTP to Activate cGAS/STING in ALS. *Cell* **183**, 636-649.e18 (2020).
78. Choi, I. *et al.* Microglia clear neuron-released α-synuclein via selective autophagy and prevent neurodegeneration. *Nat. Commun.* **11**, (2020).
79. Bieri, G. *et al.* LRRK2 modifies α-syn pathology and spread in mouse models and human neurons. *Acta Neuropathol.* **137**, 961–980 (2019).
80. Volpicelli-Daley, L. A. *et al.* G2019S-LRRK2 expression augments α-synuclein sequestration into inclusions in neurons. *J. Neurosci.* **36**, 7415–7427 (2016).

STAR Methods

RESOURCE AVAILABILITY

Lead contact

Further information and requests for resources and reagents should be directed to and will be fulfilled by the lead contact, Erika Holzbaur (holzbaur@pennmedicine.upenn.edu).

Data and code availability

The MS proteomics data have been deposited to the MassIVE repository with the dataset identifier MSV000090264.

EXPERIMENTAL MODEL AND SUBJECT DETAILS

Animal models

For mass spectrometry and immunoblotting analysis of brain-derived autophagic vesicles, Wildtype and GFP-LC3B transgenic mice (strain: B6Cg-Tg(CAG-EGFP/LC3)53Nmi/NmiRbrc) generated by Mizushima et al, 2004 and available from RIKEN BioResource Center in Japan (PMID 14699058), C57BL/6NTac WT and LRRK2^{G2019S} knock-in (strain: available from Taconic Models #B6 and #13940) and PINK1$^{-/-}$ (strain: B6.129S4-PINK1^{tm1Shn}/J, #017946 available from Jackson Laboratories) of both sexes at 1 month of age, 7-8months of age, or 18 months of age were euthanized according to University of Pennsylvania Institutional Animal Care and Use Committee approved procedures and the brain above the brainstem was removed and homogenized in a sucrose buffer (see method details).

Primary cell cultures

Primary mouse cortical neurons were dissected and cultured in our laboratory. Briefly, E15.5 embryos from B6NTac mice (model #B6) or homozygous LRRK2- G2019S knockin mice (model #13940) were dissected and the cortex was removed and dissociated with 0.25% trypsin and trituration. Neurons were plated in attachment media (MEM supplemented with 10% horse serum, 33 mM D-glucose and 1 mM sodium pyruvate) on poly-L-lysine coated 35 mm glass-bottom imaging dishes (P35G-1.5-20-C; MatTek). After 4-6h, media was replaced with maintenance media (Neurobasal [GIBCO] supplemented with 2% B-27 [GIBCO], 33 mM D-glucose [Sigma], 2 mM GlutaMAX [GIBCO], 100 U/mL penicillin and 100 mg/mL streptomycin [Sigma]). AraC (1 µM) was added the day after plating to prevent glia cell proliferation. Every 3-4 days, 40% of the media was replaced with fresh Maintenance Media and at DIV14 the neurons were used for biochemical analysis. For MLi-2 treatment, neurons were incubated in 100 nM MLi-2 over 72 hours or DMSO control.

Dorsal root ganglion neuron isolation and culture from mice was performed in the laboratory. Briefly, Dorsal root ganglion (DRG) cultures from adult mice were dissociated with 100 U of papain (Worthington #LS003126) followed by 1 mg/ml collagenase-II (Gibco 17101-015) and 1.2 mg/ml dispase (Roche 165859). The ganglia were then triturated in HBSS (10 mM glucose, and 5 mM HEPES; pH 7.35). Neurons were purified through 20% Percoll, plated on PLL coated plates supplemented with laminin (BD biosciences 354232), and cultured in F-12 media (GibcoBRL 11765-047) with 10% heat-inactivated fetal bovine serum, 100 U/mL penicillin, and 100 µg/mL streptomycin.

METHOD DETAILS

Isolation of autophagic vesicles by differential centrifugation

Enriched autophagosome fractions were isolated following a protocol modified from Strømhaug et al., 1998 and Maday et al., 2014. Briefly, one mouse brain or ~15 million neurons were collected in a 250mM sucrose solution buffered with 10μM HEPES and 1mM EDTA at pH 7.3, homogenized using a tissue grinder, incubated with Gly-Phe-β-naphthylamide (GPN) for 7 min at 37°C to destroy lysosomes and subsequently subjected to three differential centrifugations through 9.5% Nycodenz and 33% Percoll and 30% Optiprep discontinuous gradients to isolate vesicles of the appropriate size and density. Following collection, the autophagic vesicle enriched fraction (AV) was divided into three, one third was treated with 10μg Proteinase K for 45min at 37°C, similar to Le Guerroué et al., 2017 and Zellner et al., 2021, to degrade non-membrane protected proteins and enrich for internal autophagosome cargo (AV+PK), one third was membrane permeabilized by the addition of 0.2% Triton X-100 prior to the same proteinase K treatment as a negative control (AP+Tx+PK), and the other third was left untreated for identification of all internal and externally-associated proteins on autophagosomes. AV-enriched fractions were subsequently used for mass spectrometry, electron microscopy, immunoblotting and confocal microscopy.

Proteomics – sample preparation and digestion

The AV and AV+PK fractions from independent mouse brain preparations were lysed with RIPA buffer (50 mM HEPES (pH 7.4), 150 mM NaCl, 1% sodium deoxycholate, 1% NP-40, 0.1% SDS, 2.5 mM MgCl2, 10 mM sodium glycerophosphate, 10 mM sodium biphosphate) containing 1 μg/ml aprotinin, 1 μg/ml leupeptin, 1 mM benzamidine, 1 mM AEBSF and 1% final SDS. Lysates were sonicated on ice three times, followed by centrifugation (13000 rpm, 5 min). Protein concentration was measured by Bradford assay. Protein extracts (50 ug) were subjected to disulfide bond reduction with 5 mM TCEP (room temperature, 10 min) and alkylation with 25 mM chloroacetamide (room temperature, 20 min) and followed by TCA precipitation, prior to protease digestion. Samples were resuspended in 100 mM EPPS, pH 8.5 containing 0.1% RapiGest and digested at 37°C for 8 h with Trypsin at a 100:1 protein-to-protease ratio. Trypsin was then added at a 100:1 protein-to-protease ratio and the reaction was incubated for 6 h at 37°C. Following incubation, digestion efficiency of a small aliquot was tested. The sample was vacuum centrifuged to near dryness, resuspended in 5% formic acid for 15 min, centrifuged at 10000×g for 5 minutes at room temperature and subjected to subjected to C18 StageTip desalting.

Proteomics – Liquid chromatography and tandem mass spectrometry

Mass spectrometry data were collected using an Orbitrap Eclipse Tribrid Mass Spectrometer (Thermo Fisher Scientific), combined with a high-field asymmetric waveform ion mobility spectrometry (FAIMS) Pro interface, coupled to a Proxeon EASY-nLC1000 liquid chromatography (LC) pump (Thermo Fisher Scientific). Peptides were separated on a 100 μm inner diameter microcapillary column packed in house with ~35 cm of Accucore150 resin (2.6 μm, 150 Å, Thermo Fisher Scientific, San Jose, CA) with a gradient (ACN, 0.1% FA) over a total 60 min run at ~550 nL/min. For analysis, we loaded 1/4 of each fraction onto the column. The scan sequence began with an MS^1 spectrum (Orbitrap analysis resolution 120,000 at 200 Th; mass range 375−1500 m/z; automatic gain control (AGC) target 4×10^5; maximum injection time 50 ms) and peak-picking algorithm Advanced Peak Determination was used. Precursors for MS^2 analysis were selected using a cycle type of 1 sec/CV method (FAIMS CV=-40/-60/-80 (Schweppe et al., 2019)). MS^2 analysis consisted of collision-induced dissociation (quadrupole ion trap analysis; Rapid scan rate; AGC 2.0×10^4; isolation window 0.7 Th; normalized collision energy (NCE) 35; maximum injection time 35 ms). Monoisotopic peak assignment was used, determined charge states between 2 and 6 were required for sequencing, previously interrogated precursors were excluded

using a dynamic window (60 s ± 10 ppm) and dependent scan was performed on a single charge state per precursor.

Proteomics - Data analysis

Mass spectra were processed using Protein Discoverer using the Minora algorithm (set to default parameters). Database searching included all canonical entries from the mouse Reference Proteome UniProt database (SwissProt – 2019-12), as well as an in-house curated list of contaminants. The identification of proteins was performed using the SEQUEST-HT engine against the database using the following parameters: a tolerance level of 10 ppm for MS^1 and 0.6 Da for MS^2 post-recalibration and the false discovery rate of the Percolator decoy database search was set to 1%. Trypsin was used as the digestion enzyme, two missed cleavages were allowed, and the minimal peptide length was set to 7 amino acids. Carbamidomethylation of cysteine residues (+57.021 Da) were set as static modifications, while oxidation of methionine residues (+15.995 Da) was set as a variable modification. Final protein-level FDR was set to 1%. Precursor abundance quantification was determined based on intensity and the minimum replicate feature parameter was set at 50%. Proteins were quantified based on unique and razor peptides.

Protein quantification values were exported for further analysis in Microsoft Excel and Perseus (Tyanova et al., 2016)and statistical test and parameters used are indicated in the corresponding Supplementary Data Tables datasets. Briefly, Welch's t-test analysis was performed to compare two datasets, using s0 parameter (in essence a minimal fold change cut-off) and correction for multiple comparison was achieved by the permutation-based FDR method, both functions that are built-in in Perseus software.

Plasma collection

Blood from mice was collected following IACUC-approved euthanasia and decapitation. Approximately 200µl of blood was collected in a microvette tube coated in EDTA, and the samples were spun at 2000xg for 5 minutes at room temperature. 80µl of plasma was collected, diluted in 200µl PBS and denaturing buffer was added to a 1x final concentration, then boiled for 5 min at 95°C.

Immunoblotting

Samples were lysed in RIPA buffer (50 mM Tris-HCl, 150 mM NaCl, 0.1% Triton X-100, 0.5% deoxycholate, 0.1% SDS, 2x Halt Protease and Phosphatase inhibitor, PMSF, Pepstatin A, TAME and Leupeptin), centrifuged at 18,000g for 20min to clear unlysed and membranaous fractions, and then the protein concentration was determined by Bradford assay. Conditioned media from DIV14 primary cortical neurons was first pulse spun to remove cell debris in the media (5000xg for 2min) before 4x denaturing buffer was added, and boiled for 5 min at 95°C.

Proteins were resolved on 6%, 8%, 10%, 12% or 15% SDS-PAGE gels, based on size of proteins to be identified. Proteins were transferred to Immobilon-FL PVDF membranes (Millipore) using a wet blot transfer system (BioRad). 15% gels were transferred in buffer containing 20% methanol. Membranes were stained for total protein using Li-Cor Revert Total Protein Stain. Following imaging, the total protein was destained, blocked for 5min at RT with EveryBlot blocking buffer (BioRad) and incubated with primary antibodies diluted in TrueBlack WB antibody diluent + 0.2% Tween-20 overnight at 4°C. Membranes were washed three times in TBS+ 0.1% Tween-20 and incubated with secondary antibodies (1:20,000 dilution) in TrueBlack WB antibody diluent + 0.2% Tween-20 + 0.1% SDS for 1hr at RT. Following three washes in TBS+ 0.1% Tween-20,

membranes were imaged using Odyssey CLx Infrared Imaging System (LI-COR), and quantification of protein levels was performed using ImageStudio (Li-Cor).

For quantification of immunoblot data, an independent biological replicate is defined as a separate brain or cortical neuron preparation. Data was excluded if the total protein levels were unquantifiable.

Electron microscopy

AV were pelleted and fixed with 2.5% glutaraldehyde, 2.0% paraformaldehyde in 0.1M sodium cacodylate buffer, pH 7.4, overnight at 4°C. Fixed samples were then transferred to the Electron Microscopy Resource Laboratory at the University of Pennsylvania, where all subsequent steps were performed. After buffer washes, the samples were post-fixed in 2.0% osmium tetroxide for 1 hr at room temperature and then washed again in buffer, followed by dH_2O. After dehydration through a graded ethanol series, the tissue was infiltrated and embedded in EMbed-812 (Electron Microscopy Sciences, Fort Washington, PA). Thin sections were stained with lead citrate and examined with a JEOL 1010 electron microscope fitted with a Hamamatsu digital camera and AMT Advantage image capture software. Regions of dense AVs were chosen for imaging. Biological replicates are defined as separate brain-derived AV preparations.

Immunocytochemistry of DRGs

DRGs at DIV2 were fixed 1:1 in media with Bouin's solution containing 8% sucrose warmed to 37°C for 30min at RT, then washed twice in PBS before permeabilizing in 100% ice-cold methanol for 8 minutes at -20°C. The cells were washed in PBS twice before blocking in sterile filtered 0.5% goat serum + 1% BSA in PBS. Antibodies to LC3 (1:250), LAMP1 (1:20), and α-synuclein (1:5000) were diluted in blocking buffer and incubated for 1hr at RT. Following three 5min washes in PBS, secondary antibodies at 1:400 dilution in blocking buffer were incubated at RT for 1hr. Cells were stained with Hoescht (diluted to 1x) for 10min at RT before a final wash in PBS and mounted in Prolong Gold.

Thioflavin T assay

Total brain samples and AV fractions from 6 independent biological replicates were generated as described above. 5mM stock of ThT (Sigma) was resuspended in PBS and filtered through a 0.2µm syringe before use, and stored in the dark. BSA at concentrations ranging from 1-5mg/mL was resuspended in PBS and sterile filtered. Some was aggregrated by incubation at 75°C for 90min. BSA was diluted to 100 µg/µL before reading with 20µM ThT. BL and AV samples were diluted to the same protein concentration before incubation with 20µM ThT and reading in a black walled, clear bottom microplate at 450/15 485/15. Technical triplicates were performed per biological replicate. PBS only and PBS+ThT negative controls were included.

qPCR

Total brain samples from three independent biological replicates were DNA extracted using Trizol, and qPCR was performed using the Luna Universal qPCR master mix and protocol, with 50ng DNA and final primer concentration of 0.25µM. For each biological replicate, 3 technical replicates were performed. The plate reader and analysis was performed using the QuantStudio 3 Real-Time PCR System controlled by QuantStudio Design and Analysis Software (ThermoFisher Scientific).

QUANTIFICATION AND STATISTICAL ANALYSIS

Mitochondrial annotations and sublocalizations were performed using the MitoCarta3.0 and UniProt databases (Calvo et al., 2016).

GraphPad prism software (v9.1.0) was used for statistical analysis. The statistical test performed for all immunoblot analyses is unpaired t test for comparisons of two categories, or Ordinary one-way ANOVA with Šídák's multiple comparisons test for comparisons of three or more groups. Biological replicates (n), defined in the method details, are always displayed as individual data points and the precision measures (mean ± SEM) are displayed. Significance was defined as a p-value < 0.05, and directly reported in the figure. R (v4.0.4) was used to generate volcano plots, Euler diagrams and XY plots of Log_2 change of mass spectrometry data sets. Enrichr (Chen et al., 2013; Kuleshov et al., 2016; Xie et al., 2021) and SynGO (Koopmans et al., 2019) were used to compute the p-values of gene ontology term enrichment. Proteins identified as significantly changed between groups by analysis on Perseus were input into the softwares – the p-value calculation is dependent on Fisher's exact test and the q-value displays the Benjamini-Hochburg multiple hypothesis testing correction. Enrichr precomputes a background expected rank for each term in the gene set library. Neither software takes into account the background protein expression levels in specific organs.

KEY RESOURCES TABLE

REAGENT or RESOURCE	SOURCE	IDENTIFIER
Antibodies		
LC3 Rabbit polyclonal antibody (for IB)	Novus Biologicals	NB100-2220; RRID:AB_10003146
LC3 Rabbit polyclonal antibody (for ICC)	Abcam	Ab48394; RRID:AB_881433
GFM2 Rabbit polyclonal antibody	Abcam	Ab229463, lot GR3230386-2
mtTFA (TFAM) Rabbit monoclonal antibody	Abcam	Ab252432
FIS1 Mouse monoclonal antibody	Santa Cruz	sc-376447; RRID:AB_11149382
BNIP3 Mouse monoclonal antibody	Santa Cruz	Sc-56167; RRID:AB_2066767
BCL2L13 Rabbit polyclonal antibody	ProteinTech	16612-1-AP; RRID: RRID:AB_1850928
MFN2 Mouse monoclonal antibody	Santa Cruz	Sc-515647; RRID:AB_2811176
MFF Mouse monoclonal antibody	Santa Cruz	Sc-398617; RRID:AB_2744543
HUWE1 Rabbit recombinant monoclonal antibody	Abcam	Ab271032
WIPI2 Mouse monoclonal antibody	Abcam	AB105459; RRID:AB_10860881
NOS1 Mouse monoclonal antibody	Santa Cruz	Sc-5302; RRID:AB_626757
SRM Rabbit polyclonal antibody	Bethyl Laboratories	A305-505A-T lot1
MAT2A Rabbit polyclonal antibody	Novus Biosciences	NB-110-9415855; RRID:AB_1237164
GABARAPL2 Rabbit antibody	Cell Signaling Technologies	CST14256
TSG101 Mouse monoclonal antibody	BD Biosciences	612696; RRID:AB_399936
PIKFYVE (PIP5K3) Rabbit polyclonal antibody	ProteinTech	1336-1-1-AP; RRID:AB_10638310
hnRNPK Mouse monoclonal antibody	Santa Cruz	Sc-28380 Lot#A1521; RRID:AB_627734
GLA Rabbit antibody	Sigma Aldrich	HPA000237; RRID:AB_1078968
SCARB2 Rabbit polyclonal antibody	LSBio	LS-B305; RRID:AB_2182974
LGALS8 Rabbit polyclonal antibody	Abcam	Ab42879; RRID:AB_880161
P62/SQSTM1 Guinea Pig polyclonal antibody	American Research Products	03-GP62-C; RRID:AB_1542690
TAX1BP1 Mouse monoclonal antibody	Santa Cruz	Sc-393143

LAMP1 Rat monoclonal antibody (for IB and ICC)	Research diagnostics	RDI-MCD-107A-D4B
RagA Rabbit monoclonal antibody	Cell Signaling Technologies	CST4357; RRID:AB_10545136
α-synuclein Chicken polyclonal antibody (for IB and ICC)	Abcam	Ab190376; RRID:AB_2747764
p-129 α-synuclein Mouse antibody	Gift from the Luk Lab	
Anti-Rabbit IgG-IRDye 800CW, Donkey Polyclonal	Licor	Cat# 926-32213; RRID: AB_621848
Anti-Rabbit IgG-IRDye 680RD, Donkey Polyclonal	Licor	Cat# 926-68073; RRID: AB_10954442
Anti-Mouse IgG-IRDye 800CW, Donkey Polyclonal	Licor	Cat# 926-32212; RRID: AB_621847
Anti-Mouse IgG-IRDye 680RD, Donkey Polyclonal	Licor	926-68072; RRID:AB_10953628
Anti-Guinea Pig IgG-IRDye 680RD, Donkey Polyclonal	Licor	926-68077; RRID:AB_10956079
Anti-Chicken IgG-IRDye 680RD, Donkey Polyclonal	Licor	926-68075; RRID:AB_10974977
Anti-Sheep IgG AlexaFluor 680, Donkey Polyclonal	Invitrogen	2041656
Anti-Rat IgG IRDye 800CW, Goat Polyclonal	Licor	926-33219
Anti-Chicken IgG AlexaFluor 564, Goat Polyclonal (for ICC)	Invitrogen	A11040 Lot#1830310; RRID:AB_1500590
Anti-Rat IgG AlexaFluor 488, Goat Polyclonal (for ICC)	Invitrogen	A11006 Lot#2299157; RRID:AB_141373
Anti-Rabbit IgG AlexaFluor 647, Donkey Polyclonal (for ICC)	Invitrogen	A31573 Lot#2359136; RRID:AB_2536183
Bacterial and virus strains		
Biological samples		
Chemicals, peptides, and recombinant proteins		
PLL (mol wt 70,000 – 150,000)	Sigma-Aldrich	Cat# P1274
2.5% Trypsin	Thermo Fisher	Cat# 15090-046
Minimum essential medium (MEM)	Thermo Fisher	Cat# 11095-072
Horse serum (heat inactivated)	Thermo Fisher	Cat# 16050-122
Sodium Pyruvate	Corning	Cat# 36017004
D-Glucose solution 45%	Sigma-Aldrich	Cat# G8769
GlutaMAX	Thermo Fisher	Cat# 35050061
B27 Supplement	Thermo Fisher	Cat# 17504-044
Neurobasal medium	Thermo Fisher	Cat# 21103-049
10x HBSS	Gibco	Cat# 14185-052

Penicillin-Streptomycin	Thermo Fisher	Cat# 15140-122
AraC	Sigma-Aldrich	Cat# C6645
Papain	Worthington	#LS003126
Collagenase-II	Gibco	17101-015
Dispase	Roche	165859
Laminin	BD biosciences	354232
L-Cysteine	Sigma	Cat# C-6852
F-12 media	GibcoBRL	11765-047
Halt Protease and Phosphatase Inhibitor Cocktail	Thermo Fisher	Cat# 78442
Bradford reagent	Sigma	B6916
SDS (for proteomics)	Bio-Rad	Cat#1610302
TCEP	Gold Biotechnology	51805-45-9
Formic Acid	Sigma-Aldrich	Cat# C0267
Trypsin (for proteomics)	Promega	Cat# V511C
Rapigest SF Surfactant	Glixx Laboratories	Cat#GLXC-07089
EPPS	Sigma-Aldrich	Cat#E9502
2-Choroacetamide	Sigma-Aldrich	Cat#C0267
Empore SPE Disks C18	3M-Sigma-Aldrich	Cat#66883-U
Immobilon-FL PVDF membranes	Millipore	IPFL00010
Li-Cor Revert Total Protein Stain	Licor	926-11021
EveryBlot Blocking Buffer	BioRad	12010020
TrueBlack WB Antibody Diluent	Biotium	23013B
SYBR Gold	Invitrogen	S11494
CellMask Deep Red	Invitrogen	C10046
Percoll	Sigma	Cat#P1644
Proteinase K	Sigma	Cat#P2308
Gly-Phe-Beta-naphthylamide	Cayman Chemical	Cat#14636
Nycodenz	Cosmo Bio USA	Cat#1002424
Optiprep	Cosmo Bio USA	Cat#04-03-9392/01
Bouin's solution	Sigma	HT10132
Prolong Gold antifade reagent	Invitrogen	P36930
Thioflavin T	Sigma	T3516
Microvettre CB 300 K2E	Sarstedt	16.444.100 Lot#9074611
Critical commercial assays		
Luna Universal qPCR master mix	New England Biolabs	M3003
Deposited data		
MS proteomics	MassIVE	MSV000090264

Experimental models: Cell lines		
Experimental models: Organisms/strains		
B6Cg-Tg(CAG-EGFP/LC3)53Nmi/NmiRbrc)	Mizushima et al., Mol. Biol.Cell, 2004	RIKEN BioResource Center in Japan
B6.129S4-PINK1^{tm1Shn}/J	Jackson Laboratories	#017946
LRRK2-G2019S knock-n	Taconic	#12940
C57BL/6NTac WT	Taconic	#B6
Oligonucleotides		
Primer: L1MdTf1 Forward: TTTGGGACACAATGAAAGCA Reverse: CTGCCGTCTACTCCTCTTGG	Goldsmith et al., Neuron, 2022	
Primer: L1MdTf2 Forward: GCGAGGATGTGGAGAAAGAG Reverse: AGTTGGGGCTTCTTCTGGAT	Goldsmith et al., Neuron, 2022	
Primer: ND2 Forward: ATCCTCCTGGCCATCGTACT Reverse: ATCAGAAGTGGAATGGGGCG	Goldsmith et al., Neuron, 2022	
Primer: COXII Forward: AACCGAGTCGTTCTGCCAAT Reverse: CTAGGGAGGGGACTGCTCAT	Goldsmith et al., Neuron, 2022	
Recombinant DNA		
Software and algorithms		
Enrichr	Xie et al, Current protocols, 2021	https://maayanlab.cloud/Enrichr/
SynGO	Koopmans et al., NeuroResource, 2019	https://syngoportal.org/
FIJI	NIH, USA	https://imagej.net/Fiji
Perseus	Tyanova et al., Nature Methods, 2016	https://maxquant.net/perseus/
ImageStudio	Li-Cor	https://www.licor.com/bio/image-studio-lite/
Volocity	PerkinElmer	
Prism 9	GraphPad	https://www.graphpad.com/scientific-software/prism/
R	The R Foundation	https://www.r-project.org/
Other		
Sketch for figure preparation (v70.2)	Sketch	https://www.sketch.com/

Orbitrap Fusion Eclipse Mass Spectrometer	ThermoFisher Scientific	Cat#FSN04-10000
Easy-nLC 1200	ThermoFisher Scientific	LC140
MitoCarta 3.0	Rath et al., Nucleic Acids Research, 2020	https://www.broadinstitute.org/mitocarta/mitocarta30-inventory-mammalian-mitochondrial-proteins-and-pathways

990

Graphical Abstract

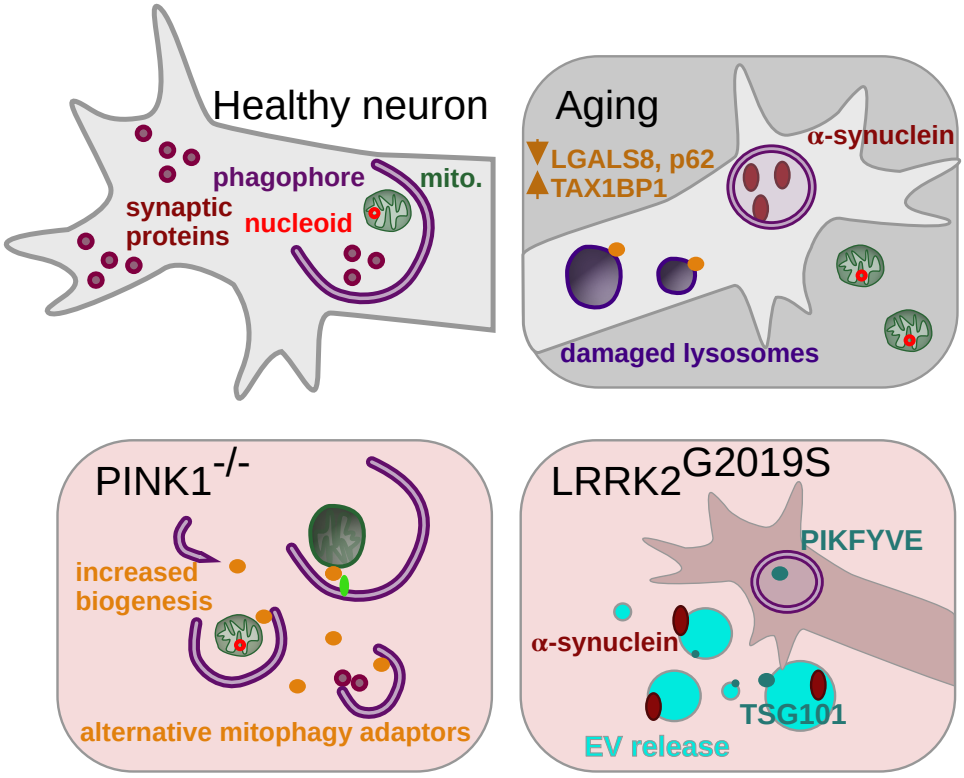

Figure 1

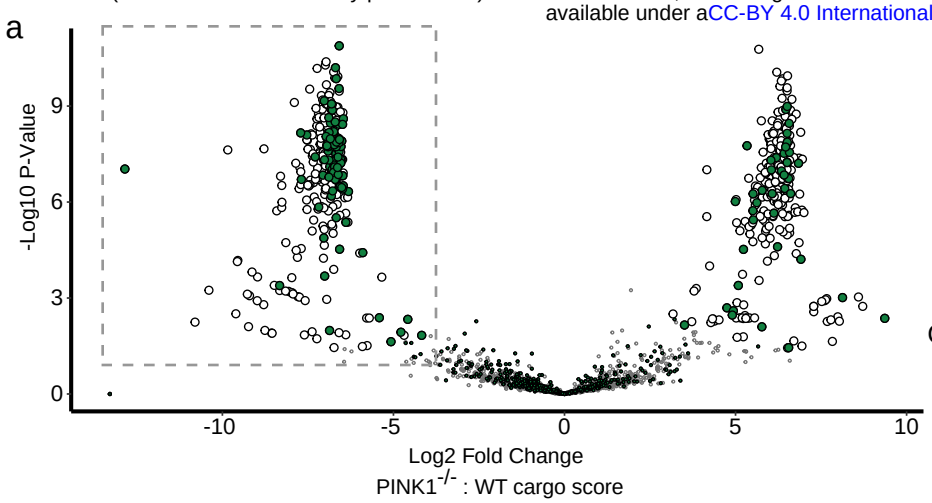

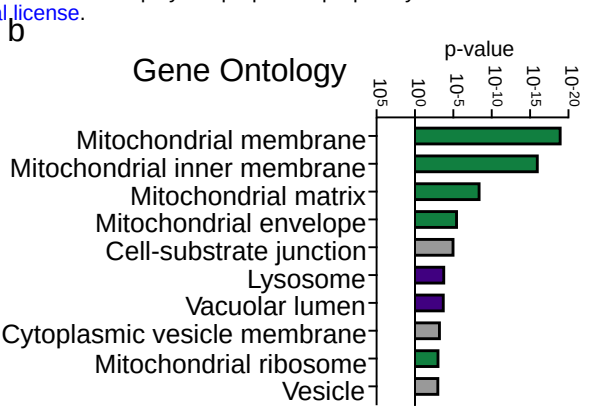

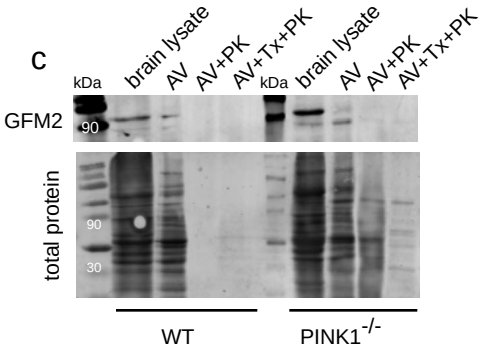

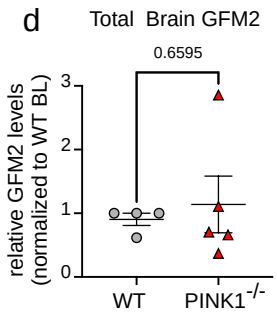

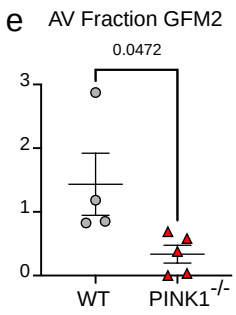

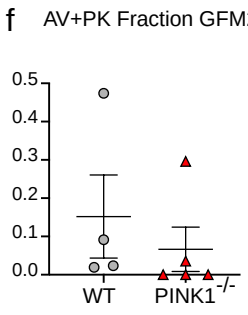

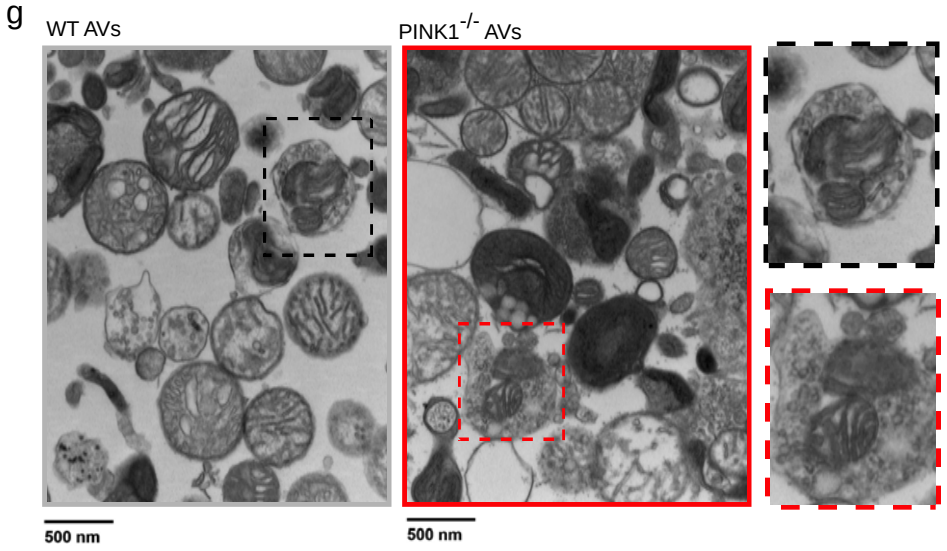

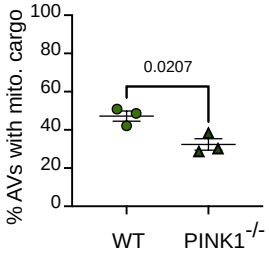

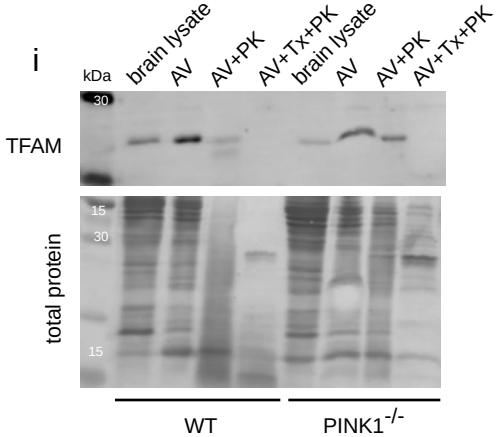

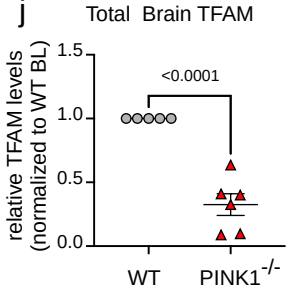

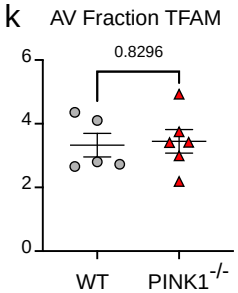

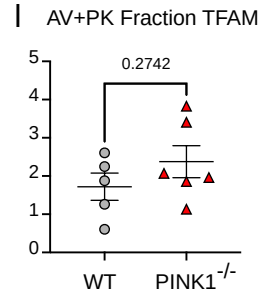

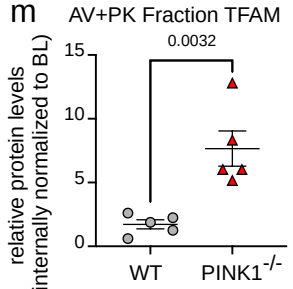

Figure 2

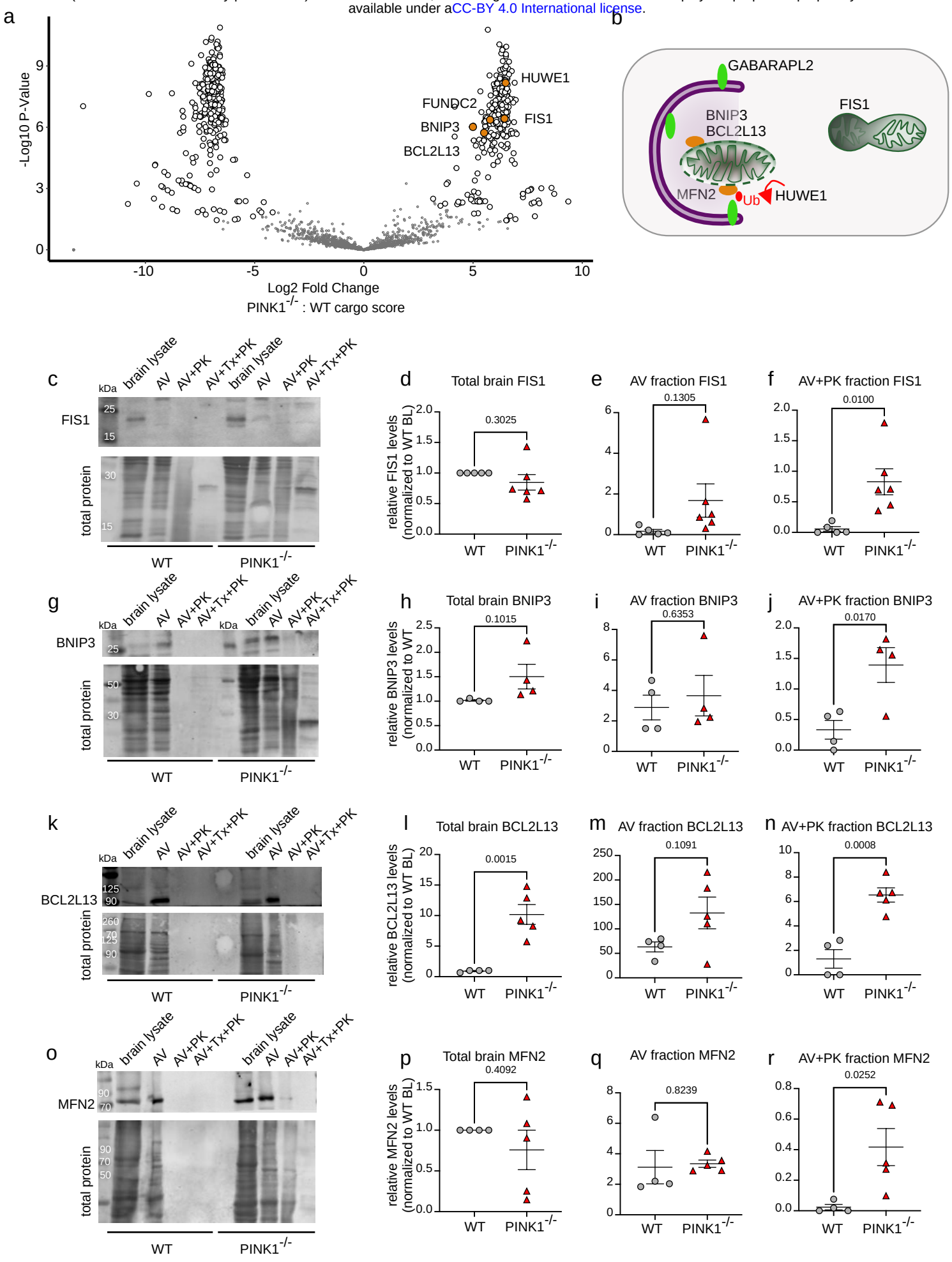

Figure 3

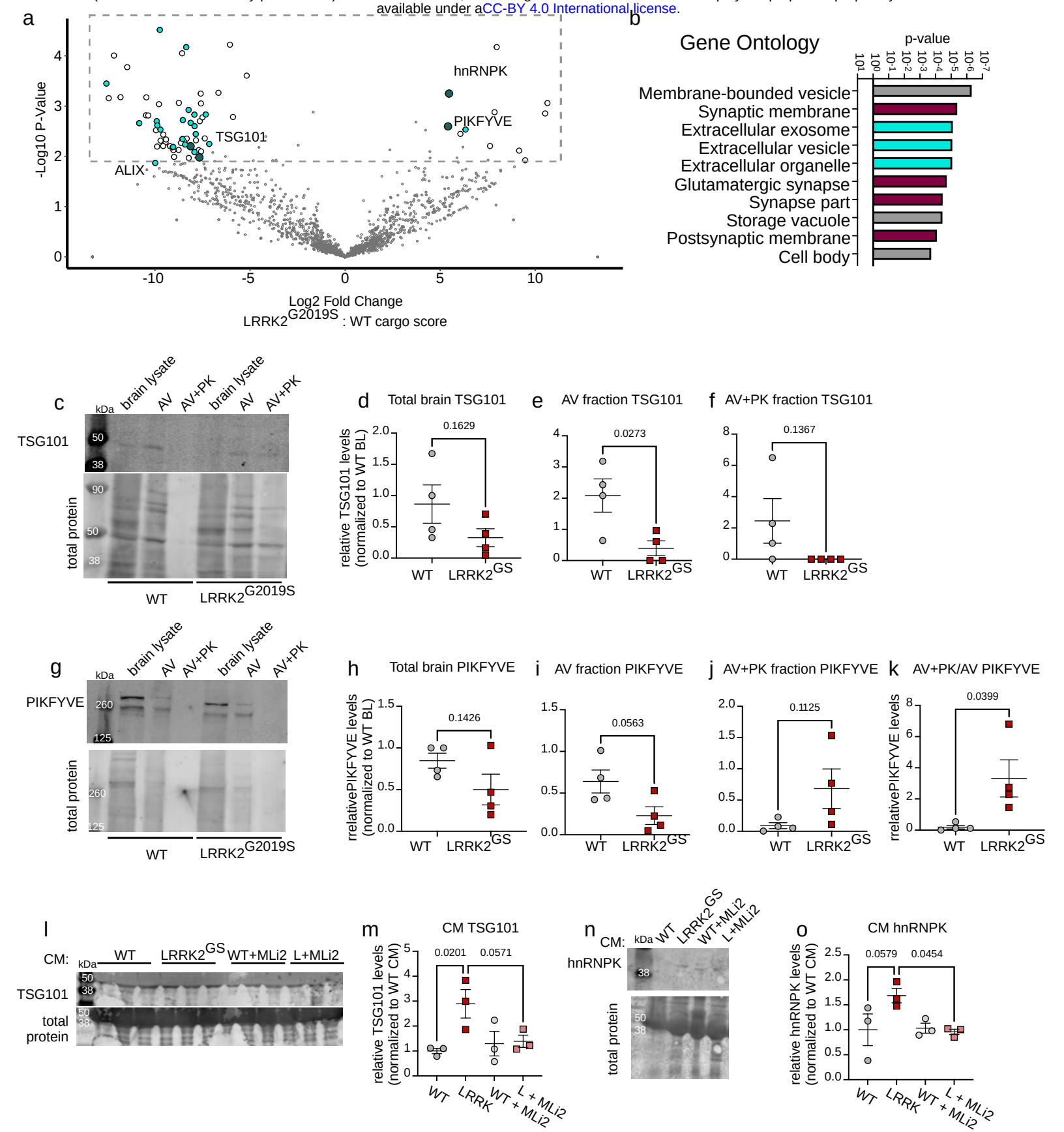

Figure 4

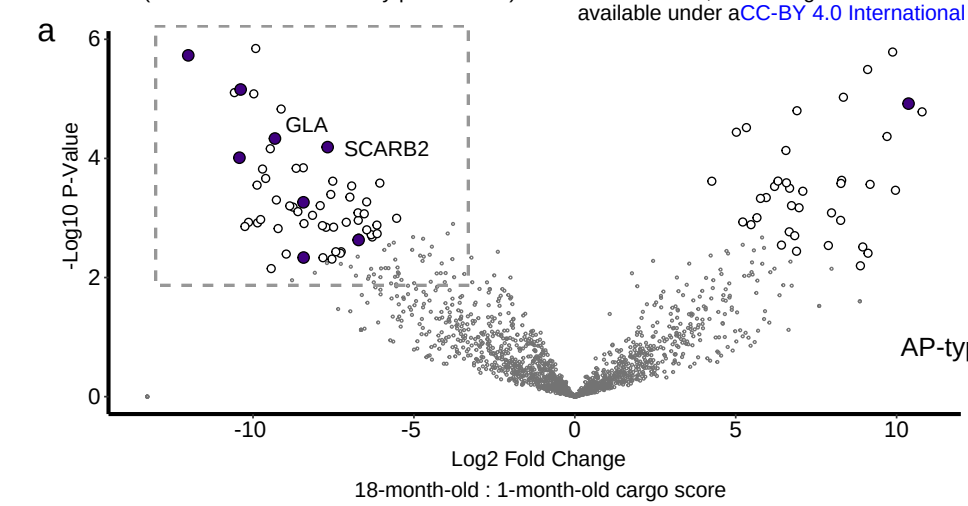

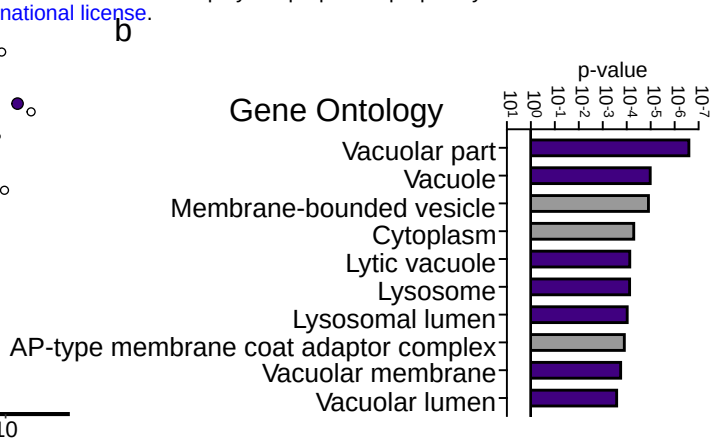

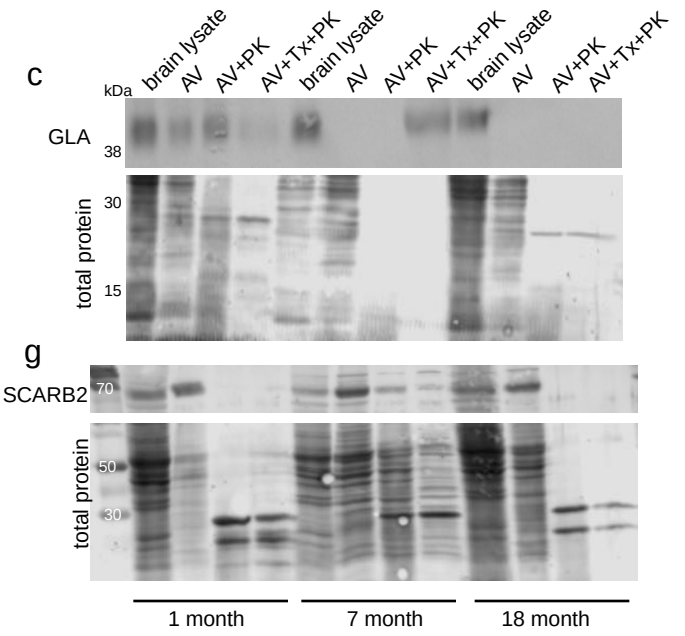

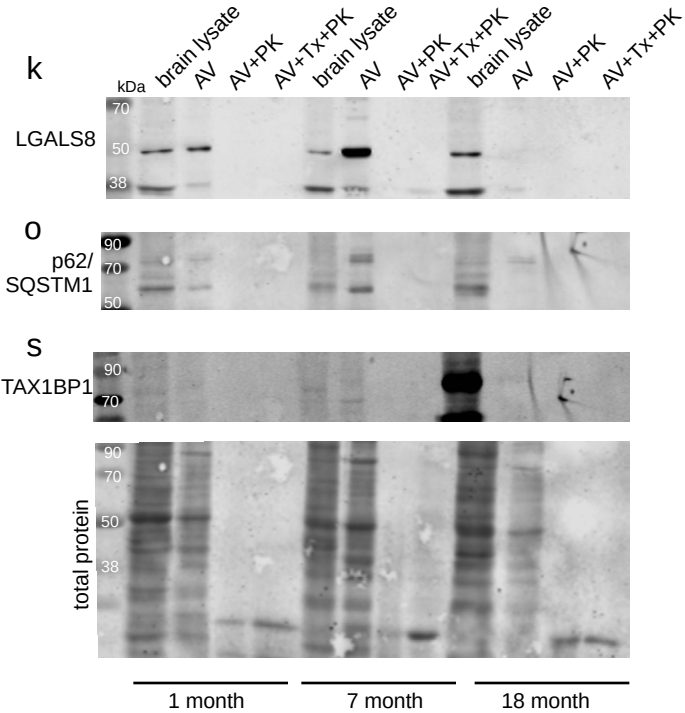

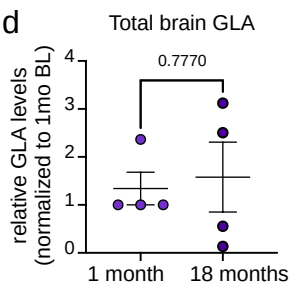

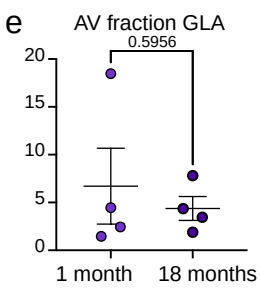

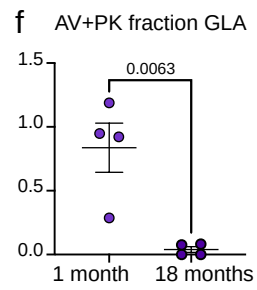

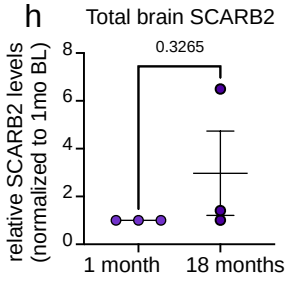

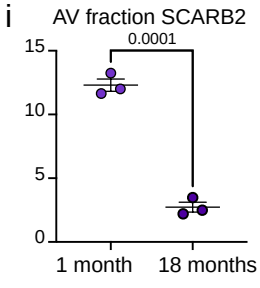

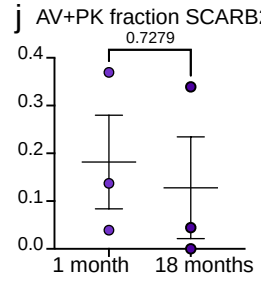

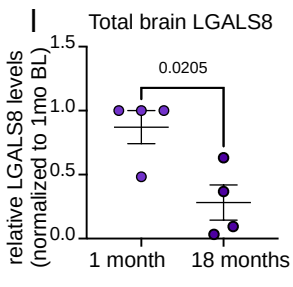

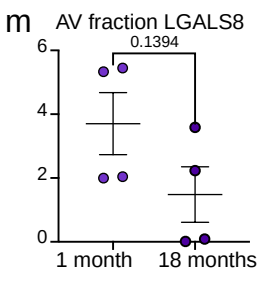

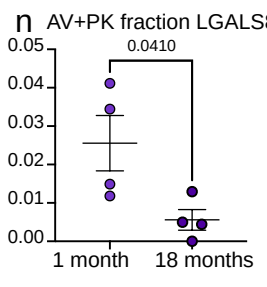

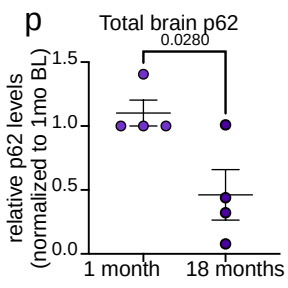

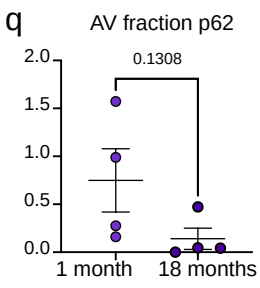

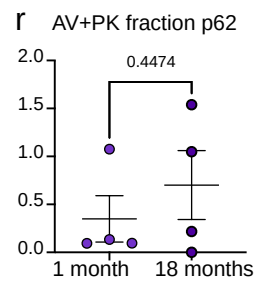

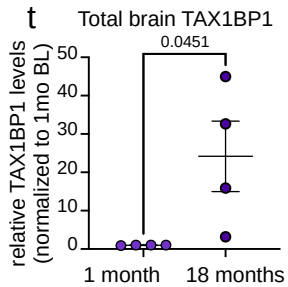

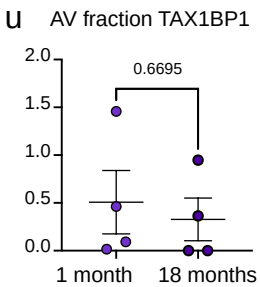

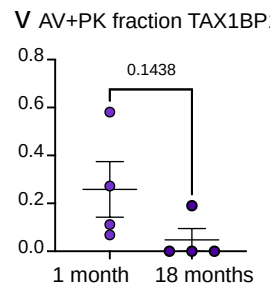

Figure 5

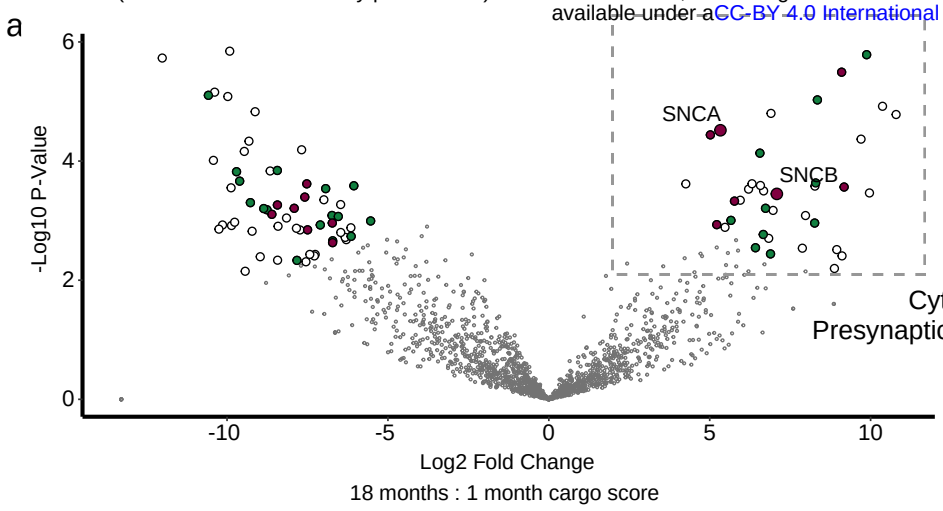

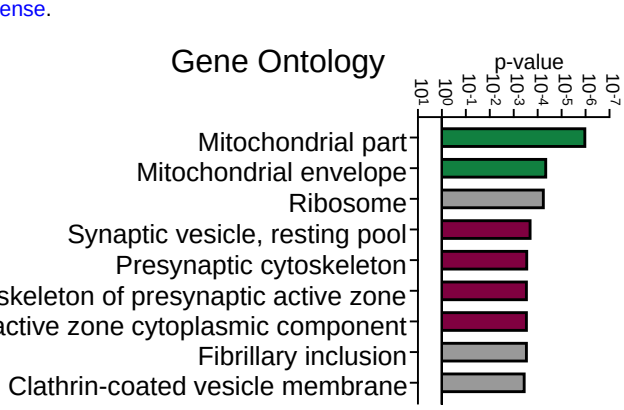

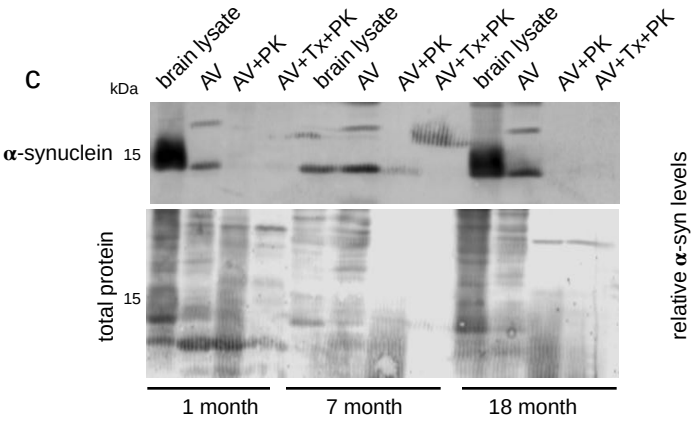

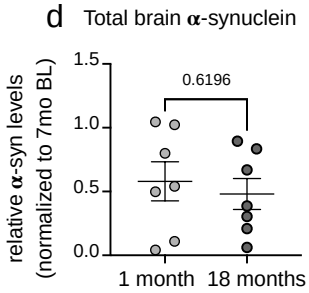

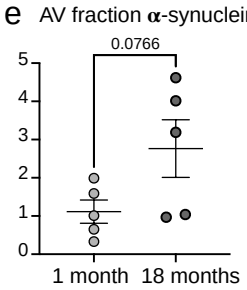

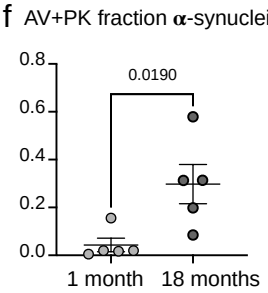

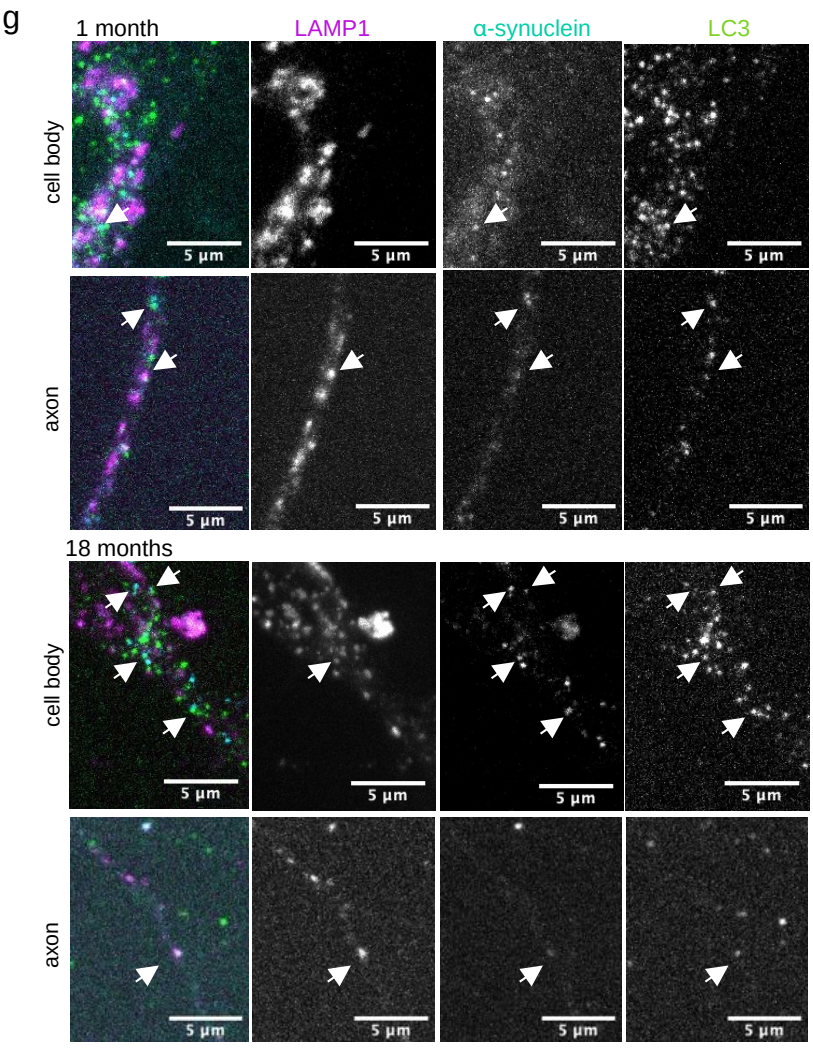

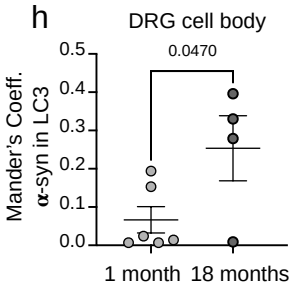

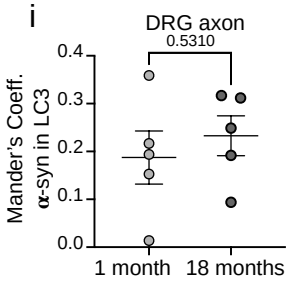

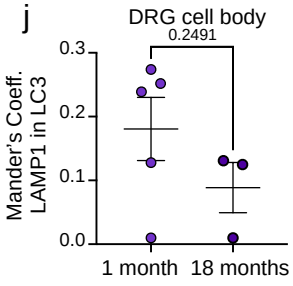

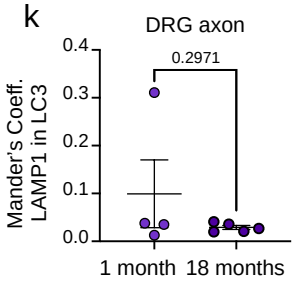

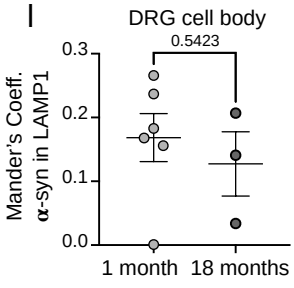

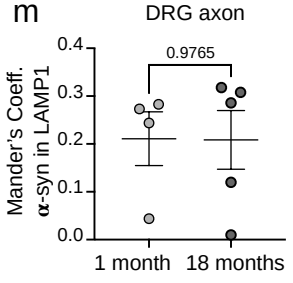

Figure 6

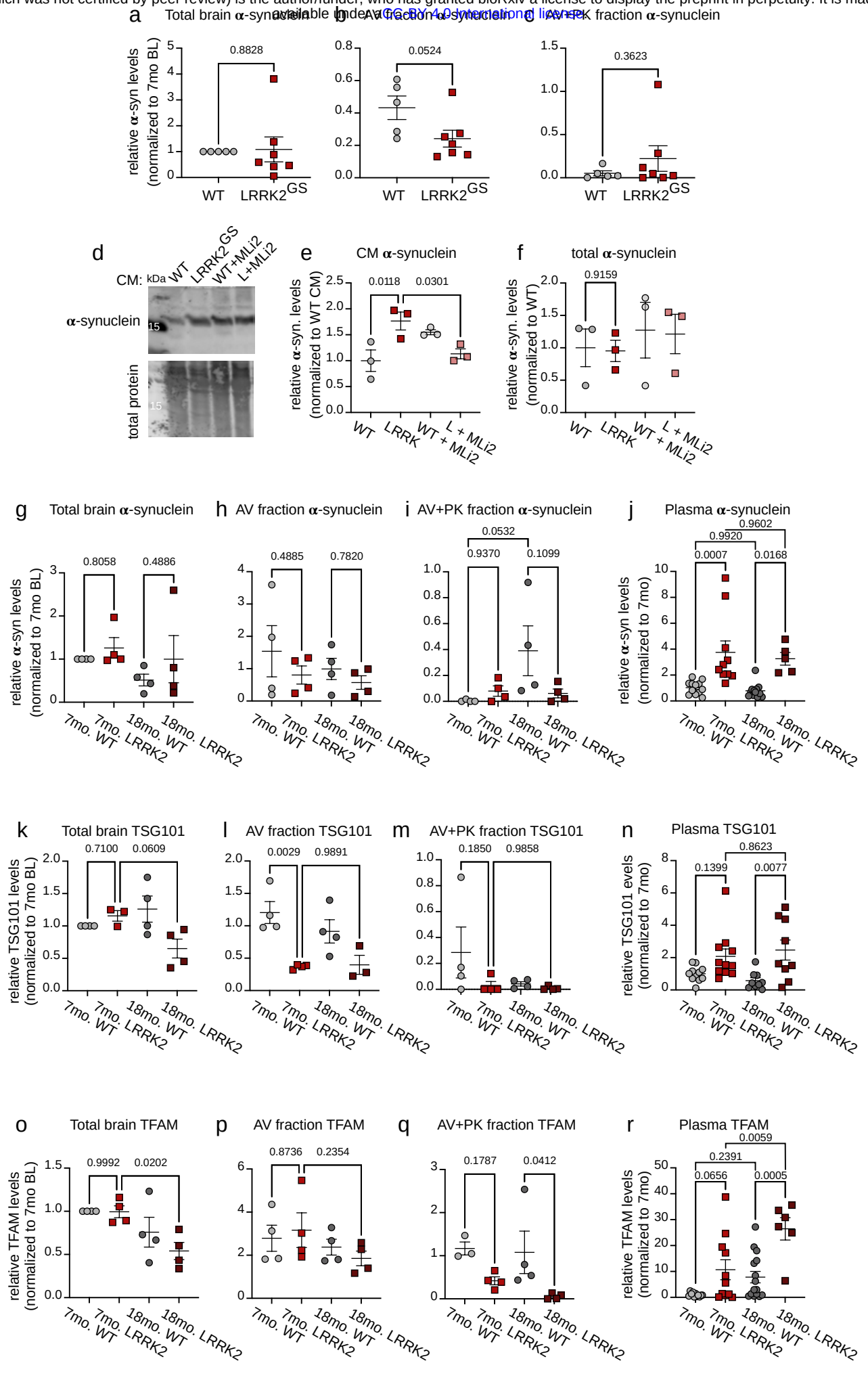

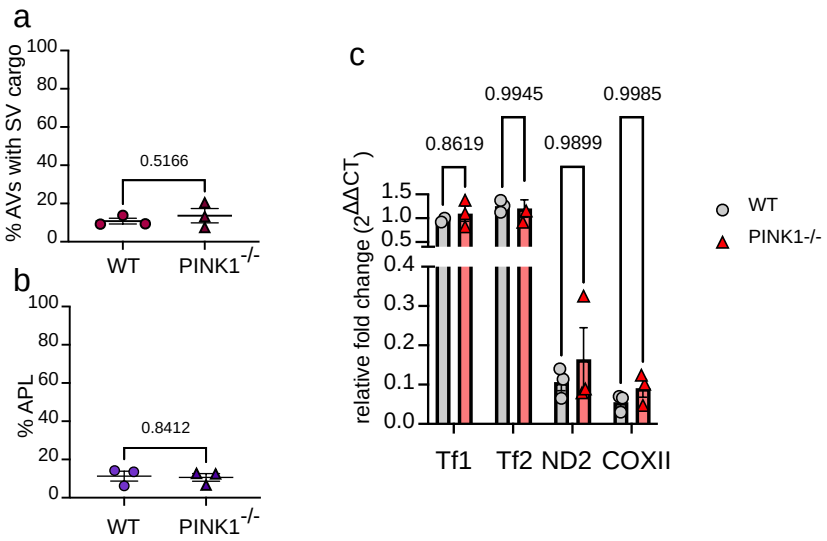

Supplementary Figure 1: PINK1$^{-/-}$ mice do not have different amounts of synaptic vesicles, autophagolyosomes in AVs, levels of mtDNA, compared to WT (related to Figure 1)

a. Quantification of AVs containing synaptic vesicle like structures from EM images (WT n=3; PINK1$^{-/-}$ n=3, >400 events counted per biological replicate). **b.** Quantification of acidified autophagolysosome structures from EM images (WT n=3; PINK1$^{-/-}$ n=3, >400 events counted per biological replicate). **c.** qPCR for nuclear DNA (LINE sequences L1MdTf1 and L1MdTf2) and mitochondrial DNA (ND2 and COXII) was performed on DNA extracted from whole brain. The relative fold change ($2^{\Delta\Delta CT}$) is plotted (mean ± SEM, WT n=3; PINK1$^{-/-}$ n=3, ANOVA with Šídák's).

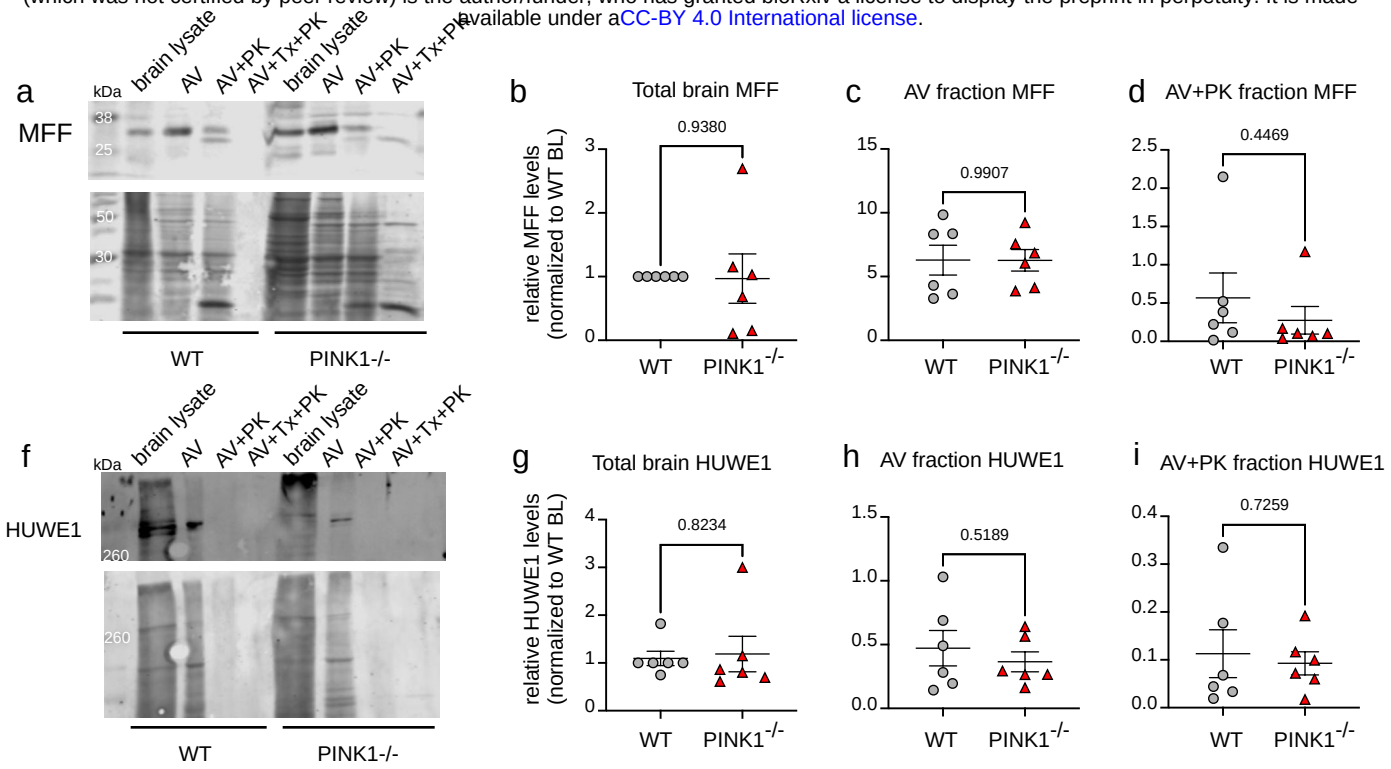

Supplementary Figure 2: MFF and HUWE1 not changed in PINK1$^{-/-}$ brain or AVs (related to Figure 2)

a-d. Representative immunoblot (**a**) and quantifications (mean ± SEM, unpaired t test) of the levels of MFF in total brain (**b**), AV fraction (**b**), and AV+PK fraction (**d**), normalized to total protein and WT total brain lysate levels. WT n=6, PINK1$^{-/-}$ n=6. **f-i.** Representative immunoblot (**f**) and quantifications (mean ± SEM, unpaired t test) of the levels of HUWE1 in total brain (**g**), AV fraction (**h**), and AV+PK fraction (**i**), normalized to total protein and WT total brain lysate levels. WT n=6, PINK1$^{-/-}$ n=6.

Supplementary Figure 3

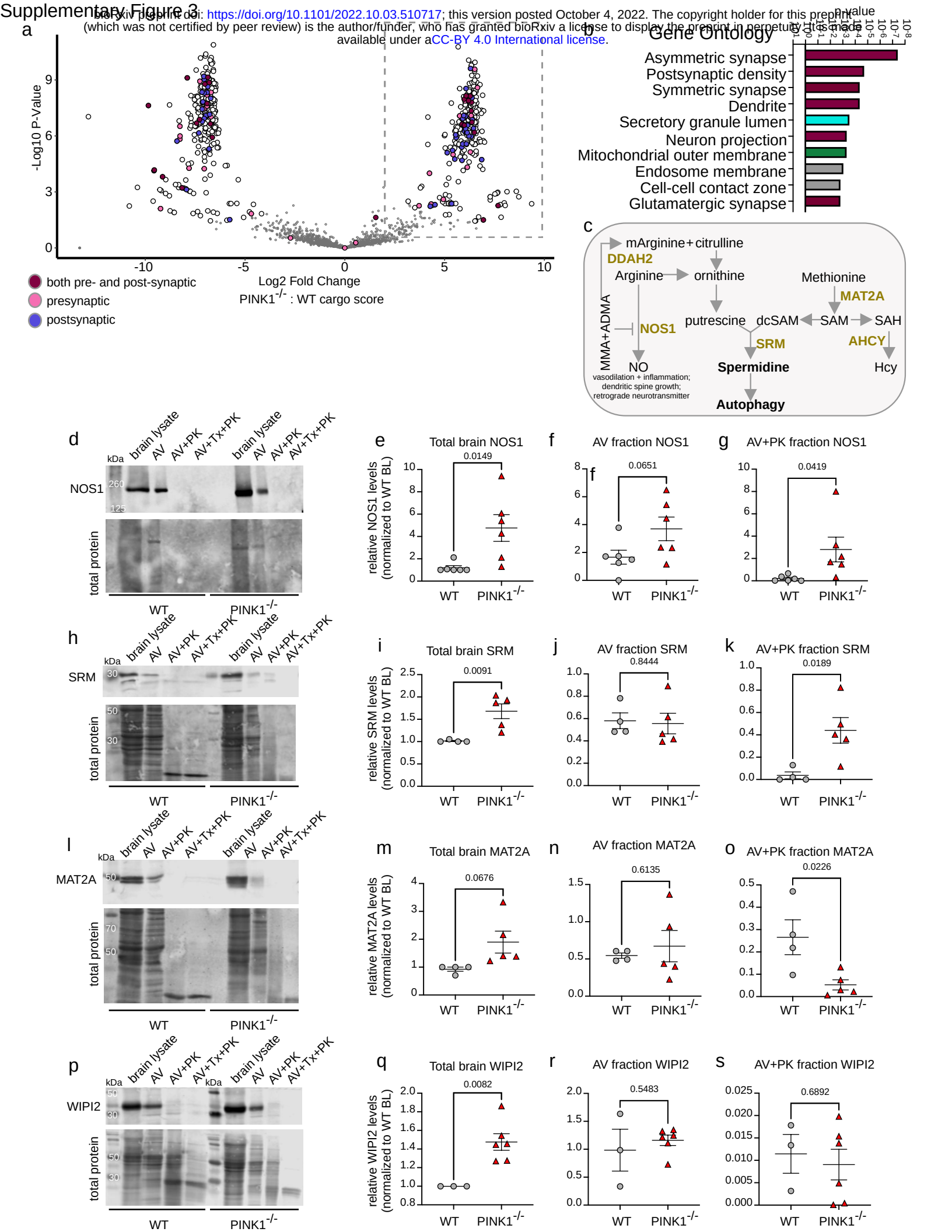

Supplementary Figure 3: Other observed changes to autophagy cargo in PINK1$^{-/-}$ AVs relative to WT include synapse related proteins and proteins in NO and spermidine synthesis

a. Identical volcano plot analysis as in Figure 1a, with presynaptic proteins highlighted in pink, post-synaptic proteins highlighted in violet, and proteins associated in both the pre and post synapse highlighted in maroon. **b.** Graph of p-values of the top gene ontology terms using the Enrichr database from proteins significantly higher in PINK1$^{-/-}$ compared to WT brain-derived AVs (the dotted box in panel a.) **c.** Diagram of nitric oxide and spermidine synthesis pathways, with proteins significantly changed as cargo in PINK1$^{-/-}$ mice highlighted in gold. **d-g.** Representative immunoblot (**d**) and quantifications (mean ± SEM, unpaired t test) of the levels of NOS1 in total brain (**e**), AV fraction (**f**), and AV+PK fraction (**g**), normalized to total protein and WT total brain lysate levels. WT n=6, PINK1$^{-/-}$ n=6. **h-k.** Representative immunoblot (**h**) and quantifications (mean ± SEM, unpaired t test) of the levels of SRM in total brain (**i**), AV fraction (**j**), and AV+PK fraction (**k**), normalized to total protein and WT total brain lysate levels. WT n=4, PINK1$^{-/-}$ n=5. **l-o.** Representative immunoblot (**l**) and quantifications (mean ± SEM, unpaired t test) of the levels of MAT2A in total brain (**m**), AV fraction (**n**), and AV+PK fraction (**o**), normalized to total protein and WT total brain lysate levels. WT n=4, PINK1$^{-/-}$ n=5. **p-s.** Representative immunoblot (**p**) and quantifications (mean ± SEM, unpaired t test) of the levels of WIPI2 in total brain (**q**), AV fraction (**r**), and AV+PK fraction (**s**), normalized to total protein and WT total brain lysate levels. WT n=3, PINK1$^{-/-}$ n=6.

Supplementary Figure 4

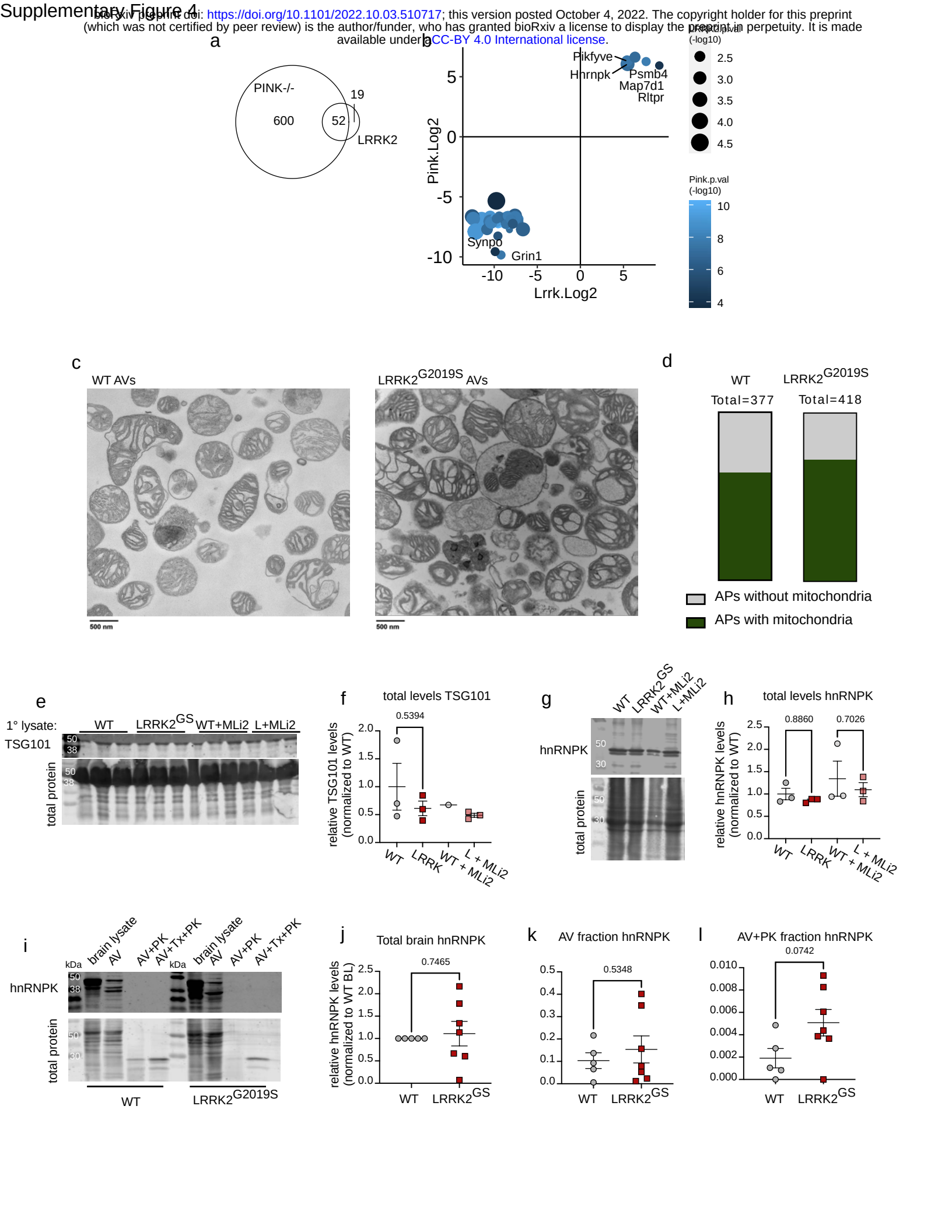

Supplementary Figure 4: LRRK2^{G2019S} AVs have some common changes to AV cargo as PINK1$^{-/-}$ but does no effect on mitochondrial fragment engulfment, and increased secretion of EVs (related to Figure 3)

a. Euler diagram of overlap of significant changes between PINK1$^{-/-}$ and WT AV cargo, and LRRK2^{G2019S} and WT AV cargo. **b.** Scatter plot showing the overlapping changes to AV cargo between PINK1$^{-/-}$ and LRRK2^{G2019S} derived AVs. Size of circle denotes the LRRK2^{G2019S} p value, and color of circle denotes the PINK1$^{-/-}$ p value. **c.** Representative electron micrographs of AVs derived from WT or LRRK2^{G2019S} mouse brains **d.** Quantification of AVs containing mitochondria from EM images. **e,f.** (**e**) Immunoblot of total levels of TSG101 in WT and LRRK2^{G2019S} primary cortical neurons, treated with DMSO or MLi2 (100nM for 72h) and (**f**) quantification (mean ± SEM, ANOVA with Šídák's) of TSG101 levels normalized to total protein and DMSO, WT control. n=3 per condition. **g,h.** (**g**) Representative immunoblot of total levels of hnRNPK in WT and LRRK2^{G2019S} primary cortical neurons, treated with DMSO or MLi2 (100nM for 72h) and (**h**) quantification (mean ± SEM, ANOVA with Šídák's) of hnRNPK levels normalized to total protein and DMSO, WT control. n=3 per condition. **i-l.** Representative immunoblot (**i**) and quantifications (mean ± SEM, unpaired t test) of the levels of hnRNPK in total brain (**l**), AV fraction (**k**), and AV+PK fraction (**l**), normalized to total protein and WT total brain lysate levels. WT n=5, LRRK2^{G2019S} n=7.

Supplementary Figure 5

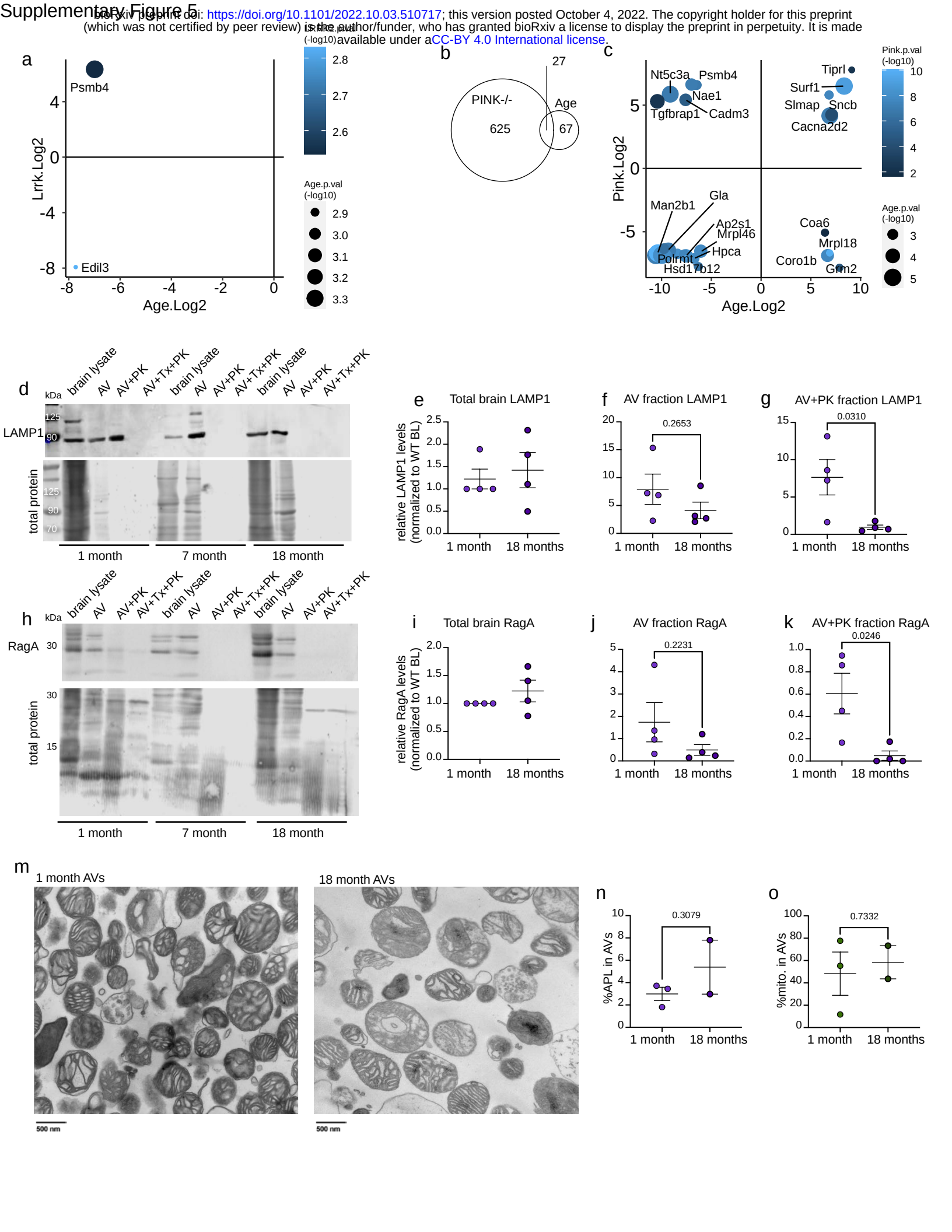

Supplementary Figure 5: Changes to AV cargo with age suggest decreases in lysophagy (related to Figure 4)

a. Scatter plot showing the overlapping changes to AV cargo between aging and LRRK2^{G2019S} derived AVs. Size of circle denotes the aging p value, and color of circle denotes the LRRK2^{G2019S} p value. **b.** Euler diagram of overlap of significant changes between PINK1$^{-/-}$ and WT AV cargo, and aging AV cargo. **c.** Scatter plot showing the overlapping changes to AV cargo between aging and PINK1$^{-/-}$ derived AVs. Size of circle denotes the aging p value, and color of circle denotes the PINK1$^{-/-}$ p value. **d-g.** Representative immunoblot (**d**) and quantifications (mean ± SEM, unpaired t test) of the levels of LAMP1 in total brain (**e**), AV fraction (**f**), and AV+PK fraction (**g**), normalized to total protein and WT total brain lysate levels. 1-month n=4, 18-month n=4. **h-k.** Representative immunoblot (**h**) and quantifications (mean ± SEM, unpaired t test) of the levels of RagA in total brain (**i**), AV fraction (**j**), and AV+PK fraction (**k**), normalized to total protein and WT total brain lysate levels. 1-month n=4, 18-month n=4. **m.** Representative electron micrographs of AVs derived from 1-month and 18-month old mouse brains. **n,o.** Quantification of (**n**) autophagolysosomes or (**o**) AVs containing mitochondria from EM images (1-month n = 3 and 18-month n = 2, >1400 events counted per condition).

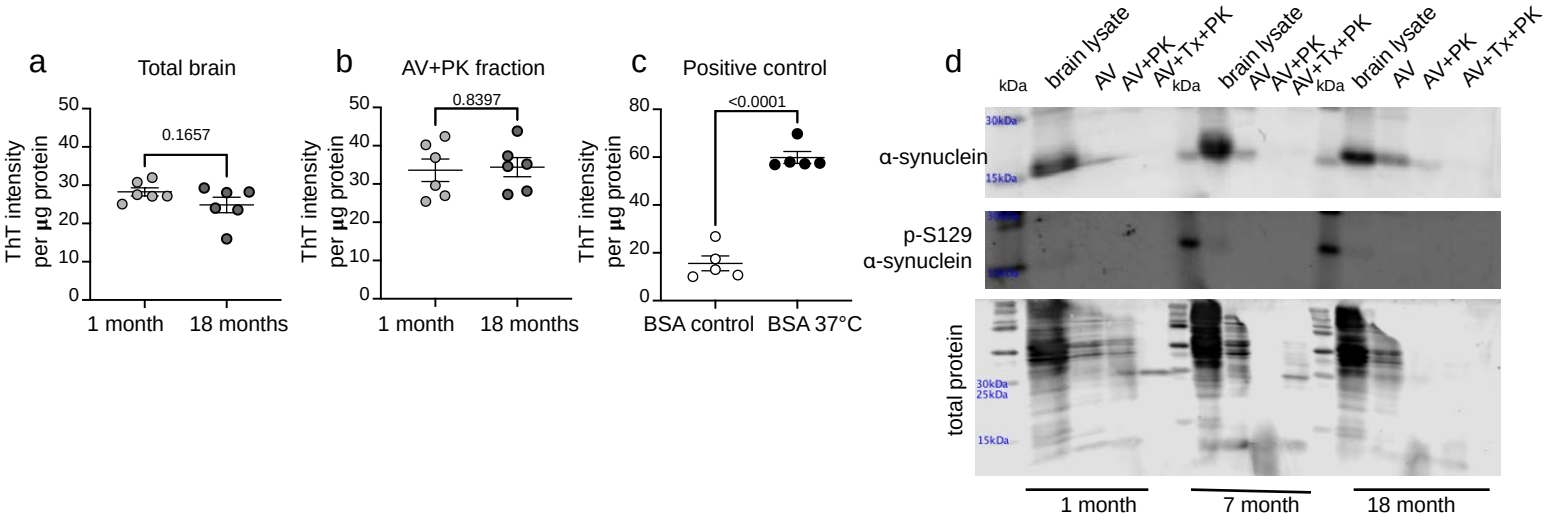

Supplementary Figure 6: No change in aggregated proteins or phosphorylated a-synuclein in AVs with age (related to Figure 5)

a-c. Quantification (mean ± SEM, unpaired t test) of Thioflavin T AU, normalized to µg protein, from (**a**) total brain fraction and (**b**) AV+PK fraction from 1-month (n=6) and 18-month (n=6) mice, and (**c**) positive control of denatured BSA (n=5). **d.** Representative immunoblot of a-synuclein and phosphorylated S129-a-synuclein from 1-month, 7-month and 18-month old mice and AV fractions, as indicated.

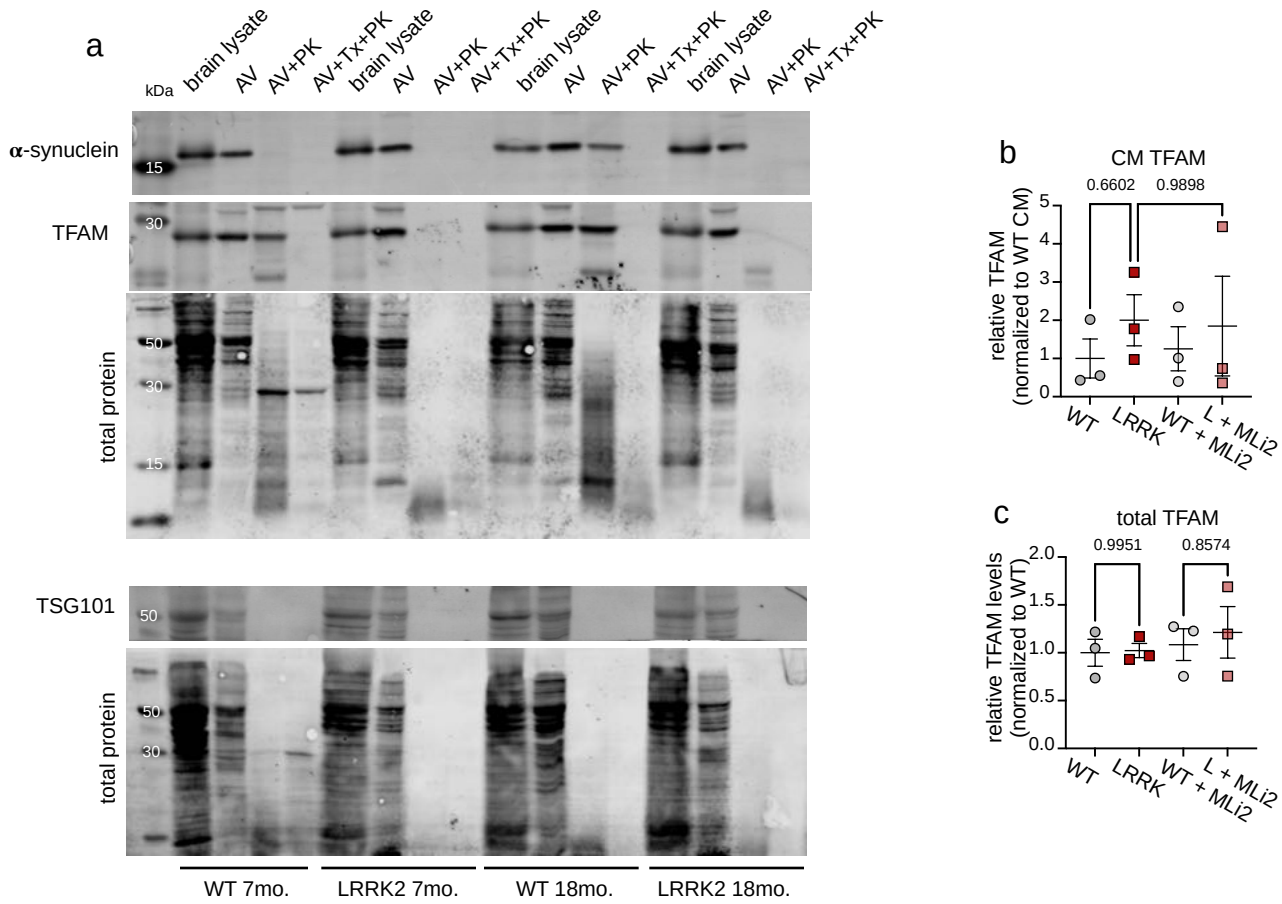

Supplementary Figure 7: (related to Figure 6)
a. Representative immunoblot of total brain and AV fractions for α-synuclein, TFAM and TSG101 from wildtype and LRRK2^{G2019S} 7-month-old and 18-month-old mice. **b,c.** Quantification (mean ± SEM, ANOVA with Šídák's) of TFAM levels, normalized to total protein and DMSO, WT control, from (**b**) conditioned media or (**c**) cell lysate from WT or LRRK2^{G2019S} primary cortical neurons, treated with DMSO or the LRRK2 kinase inhibitor MLi2 (100nM for 72h).